2. EXPLANATORY NOTES[1]

Shipboard Scientific Party[2]

INTRODUCTION

In this chapter, we have assembled information that will help the reader understand the shipboard scientific methods used to collect the data presented in the site reports in this *Initial Reports* volume of the Leg 161 *Proceedings of the Ocean Drilling Program* (ODP). Methods for shore-based analyses of Leg 161 data will be described in the individual scientific contributions to be published in the *Scientific Results* volume.

The separate sections of the site chapters were written by the shipboard scientific specialists for each scientific discipline (see Shipboard Scientific Participants list at the front of this volume).

Coring techniques and core handling, including the numbering of sites, holes, cores, sections, and samples were the same as those reported in previous *Initial Reports* volumes of the *Proceedings of the Ocean Drilling Program* (Fig. 1). Following Leg 161, the cores were transferred from the ship in refrigerated containers to cold storage at the Bremen Core Repository of the Ocean Drilling Program, in Bremen, Federal Republic of Germany.

LITHOSTRATIGRAPHY

The first part of this section summarizes the methods used to describe cored sedimentary sequences and the manner in which data collected manually on Visual Core Description Forms (VCDs) were summarized and condensed into computer-generated descriptions for each core. The second part of this section reviews the sedimentological classifications and terms used in the descriptions.

Visual Core Descriptions (VCDs) of Sedimentary Units

Core Description Forms

Leg 161 sedimentologists were responsible for visual core logging, smear-slide analyses, high-resolution sediment color analysis, and thin-section descriptions of sedimentary and volcaniclastic material. Detailed information recorded on section-by-section description forms (VCD sheets available from ODP) was condensed into core-by-core computer-generated descriptions that give graphic and textual summaries for each core (see Section III, "Cores," this volume).

Cores were designated using leg number, site number, hole letter, core number, and core type according to standard ODP procedures (see "Introduction" section, this chapter). The cored interval was specified in terms of meters below sea level (mbsl) and meters below seafloor (mbsf) on the basis of drill-pipe measurements (dpm), reported by the SEDCO Coring Technician and the ODP Operations Superintendent. Detailed coring summaries can be found on the CD-ROM in the back pocket of this volume. Depths were corrected for

the height of the rig floor dual elevator stool (DES) above sea level and the recovery of the mudline core to calculate water depth.

Graphic Lithology Column

The lithology of the recovered material is represented on the computer-generated core description forms by symbols representing as many as three components in the column titled "Graphic Lithology" (see lower right of Fig. 2). Where an interval of sediment or sedimentary rock is a homogeneous mixture, the constituent categories are separated by solid vertical lines, with each category represented by a symbol (Fig. 2). Constituents accounting for <10% of the sediment in a given lithology (or others remaining after the representation of the three most abundant lithologies) are not shown in the graphic lithology column, but are listed in the "Description" section of the core description form. In an interval composed of two or more sediment lithologies that are quite distinct, such as thinly interbedded or highly variegated sediments, the column is subdivided by a dashed line(s) separating the different lithologic symbols according to their relative abundances within the cored interval. Only the composition of layers or intervals exceeding 20 cm in thickness are shown on the graphic lithology column because of limitations in the software used for generating core summaries. In addition, the software does not allow for combinations of interbedded (dashed line) and mixed (solid line) lithologies within a given interval.

Age Column

The chronostratigraphic unit, as recognized on the basis of paleontological and paleomagnetic data, is shown in the "Age" column on the core summary sheets. Boundaries between assigned ages are indicated as follows:

1. Sharp boundary = straight line;
2. Unconformity or hiatus = line with "+" signs above it;
3. Uncertain = line with question marks.

Structure Column

Sedimentary structures such as cross stratification, grading, and bioturbation are indicated in the "Structure" column of the core summary sheet (Fig. 3). Core summary software also enables color banding to be indicated, but does not include symbols to record bed thickness. On Leg 161, the shipboard sedimentologists decided to use the color-banding symbols to indicate both color banding and interbedded lithologies because smear-slide and carbonate analyses indicate that color changes are associated with lithological variations. The following definitions were adopted (Blatt et al., 1980, p. 128):

1. Thick bedding/color banding = >30 cm;
2. Medium bedding/color banding = 10–30 cm;
3. Thin bedding/color banding = <10 cm.

```
-----------------------------------------------------------

While Coring
        APC in situ temperature (ADARA)
        APC core orientation (Tensor)

Between XCB cores
        In situ temperature (WSTP)

Core recovered on deck
        Curation (cut into 1.5-m sections)
        Whole-round samples for interstitial water analysis
        Head space/vacutainer (gas monitoring)
        Micropaleontology using core-catcher samples
        Bacteria sampling

Cores taken into laboratory
        Equilibrate to room temperature
        Multi-sensor track for core-core and core-log integration
                GRAPE, magnetic susceptibility, natural gamma
                radiation, compressional wave velocity
        Thermal conductivity

Core are split into working and archive halves
        Archive half
                Whole-core color and black-and-white photography
                Core description:
                        lithostratigraphy, petrology, structural geology
                Pass-through cryogenic magnetometer

        Working half
                Digital color spectrophotometer
                Physical properties (velocity, index properties, shear
                        strength)
                Organic and inorganic geochemistry
                Micropaleontology
                X-ray diffraction
                X-ray fluorescence
                Thin sections
                Sampling for post-cruise research

After coring
        Downhole logging

-----------------------------------------------------------
```

Figure 1. Generalized sequence of scientific data collection and core flow. Detailed scientific methods for each lab are described below and the detailed results from each site are reported in separate chapters in this volume.

The core-summary software allows sharp and gradational boundaries between color banding to be depicted. Banding showing one sharp boundary and one gradational boundary was arbitrarily designated as having gradational boundaries.

Disturbance Column

Sediment disturbance resulting from coring may be difficult to distinguish from natural structures. Nonetheless, it is important to estimate the amount and nature of core disturbance in the "Disturbance" column on the core summaries (using symbols in Fig. 3). Blank regions indicate no drilling disturbance. The degree of drilling disturbance is described for soft and firm sediments using the following categories:

1. *Slightly deformed:* bedding contacts are slightly bent.
2. *Moderately deformed:* bedding contacts are extremely bowed.
3. *Highly deformed:* bedding is completely disturbed, in some places showing symmetrical diapir-like or flow structures.
4. *Soupy:* intervals are water-saturated and all aspects of original bedding are destroyed.

The degree of fracturing in indurated sediments and igneous and metamorphic basement rocks is described using the following categories:

1. *Slightly fractured:* core pieces are in place and contain little drilling slurry (ground rock and water) or breccia;
2. *Moderately fragmented:* core pieces are in place or partly displaced, but the original orientation is preserved or recognizable (drilling slurry may surround fragments);
3. *Highly fragmented:* pieces are from the cored interval and probably in the correct stratigraphic sequence (although they may not represent the entire section), but the original orientation is completely lost;
4. *Drilling breccia:* core pieces have lost their original orientation and stratigraphic position and may be mixed with drilling slurry.

Color Column

The hue and chroma attributes of color were determined using Munsell Soil Color Charts (1975) and a Minolta, CM-2002 hand-held spectrophotometer. The Munsell colors were recorded in the "Color" column on the core description form. The spectrophotometer measurements were made to establish semi-quantitative relationships between spectral reflectance in distinctive wave bands and identified lithologies, in addition to providing a continuous stratigraphic record of color variations.

Spectrophotometer measurements were made every 2 cm on the working half of cores from Sites 974 and 975, and at wider increments on cores from Sites 976 and 977 as soon as possible after the core was split. The core was covered with plastic (Saran™) wrap before color analysis to protect the core from damage by the spectrophotometer. A white standard (also covered with plastic wrap) was analyzed before and after incremental measurements on each core. The spectrophotometer data are discussed in the "Composite Depths" chapter, this section. A more detailed discussion of this method of color analysis can be found in the ODP Leg 155 *Initial Reports* volume (Leg 155 Shipboard Scientific Party, 1995b).

Sample Column

The positions of samples taken from each core for shipboard analysis are indicated in the "Samples" column on the core description form, as follows:

I = interstitial water;
M = micropaleontology;
S = smear slide;
T = thin section.

Organic geochemistry and smear-slide samples were often taken from the same interval in order to calibrate petrographic estimates of total carbonate components with geochemical determinations.

Description Column

The lithologic description that appears on each core description form consists of three parts: (1) a heading that lists all the major sediment lithologies observed in the core; (2) a heading for minor lithologies, and (3) more detailed description of major and minor sediments, including features such as color, composition (smear-slide analysis), sedimentary structures, or other characteristics. Descriptions and locations of thin, interbedded, or minor lithologies that cannot be depicted in the graphic lithology column are included in this section.
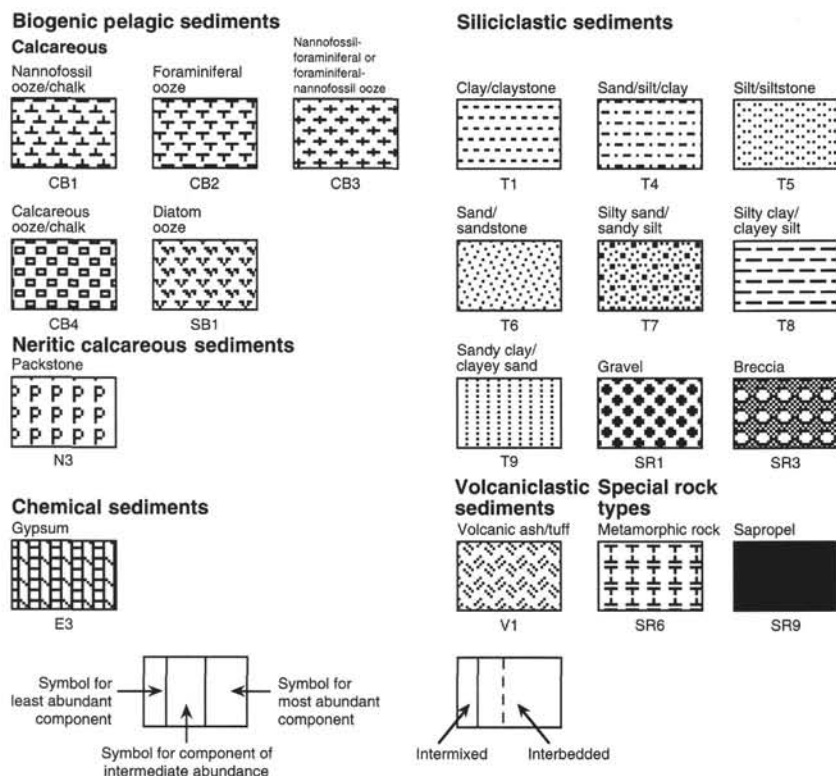
Biogenic pelagic sediments

Calcareous

Nannofossil
ooze/chalk

Foraminiferal
ooze

Nannofossil-
foraminiferal or
foraminiferal-
nannofossil ooze

CB1   CB2   CB3

Calcareous
ooze/chalk

Diatom
ooze

CB4   SB1

Neritic calcareous sediments

Packstone

N3

Chemical sediments

Gypsum

E3

Siliciclastic sediments

Clay/claystone   Sand/silt/clay   Silt/siltstone

T1   T4   T5

Sand/
sandstone

Silty sand/
sandy silt

Silty clay/
clayey silt

T6   T7   T8

Sandy clay/
clayey sand

Gravel   Breccia

T9   SR1   SR3

Volcaniclastic
sediments

Volcanic ash/tuff

V1

Special rock
types

Metamorphic rock   Sapropel

SR6   SR9

Symbol for
least abundant
component

Symbol for
most abundant
component

Symbol for component of
intermediate abundance

Intermixed   Interbedded

Figure 2. Key to symbols used in the "graphic lithology" column on the computer-generated core summaries in Section III, "Cores," this volume.

Classification of Sediments and Sedimentary Rocks

Introduction

Sedimentologists on Leg 161 used a modified version of the sediment classification scheme of the Ocean Drilling Program (Shipboard Scientific Party, 1990; Mazzullo et al., 1988) for granular sediment types (Fig. 4). Variations in the relative proportions of siliciclastic, volcaniclastic, pelagic, and neritic components define five major classes of granular sediments (Fig. 4). The neritic component consists of skeletal and non-skeletal shallow-water bioclasts, including shallow-water benthic foraminifers. Pelagic grains are the skeletal remains of open-marine siliceous and calcareous microfauna and microflora (e.g., radiolarians, diatoms, planktonic foraminifers, nannofossils) and associated organisms. Note that the term micrite is used to define very fine-grained calcareous particles (~<10 μm), of uncertain origin observed in smear slides. Carbonate content was qualitatively estimated using smear slides and quantitatively estimated by coulometric analysis (see "Organic Geochemistry" section, this chapter). Siliciclastic grains are mineral and rock fragments derived from igneous, sedimentary, and metamorphic rocks. Volcaniclastic grains include those of pyroclastic (direct products of magma degassing) and epiclastic (detritus derived from weathering and erosion of volcanic rock) origins.

Granular Sediments

A granular sediment is classified by designating a principal name and major and minor modifiers. The principal name of a granular sediment (e.g., ooze, fine sand or sandstone, volcanic breccia) defines its granular-sediment class as depicted in Figure 4; the major and minor modifiers describe the texture, composition, and fabric.

The principal name of a granular-sediment class is preceded by major and minor modifiers that describe the lithology of the granular

sediment in greater detail (e.g., a lithified siliciclastic rock composed of 55% clay, 35% quartz-silt, and 15% foraminifers is classified as a foraminifer-rich silty claystone). Major and minor modifiers, as applied in the aforementioned example, are used most commonly to describe composition and textures of grain types present in major (30%–60%) and minor (10%–30%) proportions. Major and minor modifiers may also be used to describe grain fabric (e.g., matrix supported) in siliciclastic and volcaniclastic sediment types.

Composition of pelagic grains can be described with the major and minor modifiers diatom(-aceous), radiolarian, spicule(-ar), siliceous, nannofossil, foraminifer(-al), and calcareous. The terms siliceous and calcareous are used generally to describe sediments composed of siliceous or calcareous pelagic grains of mixed origins.

Grain shape, mineralogy, rock fragment types, fabric, degree of induration, and color can be used as major modifiers. Grain shapes are described by the major modifiers rounded, subrounded, subangular, and angular. The character of siliciclastic grains can be described by mineralogy (using modifiers such as "quartzose" "feldspathic," "glauconitic," "micaceous," "zeolitic," "lithic," or "calcareous." Modifiers such as volcanic, sed-lithic, meta-lithic, gneissic, and plutonic, which describe the provenance of rock fragments, can also be used in the classification of sediments (particularly in gravels, conglomerates, and breccias). The fabric of a sediment can be described as well using major modifiers such as grain-supported, matrix-supported, and imbricated. Generally, fabric terms are useful only when describing gravels, conglomerates, and breccias. The degree of lithification is described using the following major modifiers: "unlithified" designates soft sediment that is easily deformed when touched, "partially lithified" designates firm sediment that is incompletely lithified, and "lithified" designates hard, cemented sediment that must be cut with a saw. Degree of lithification was determined for wet core. Finally, sediment color, as determined visually with the Munsell Color Chart (1975), can also be employed as a major modifier.
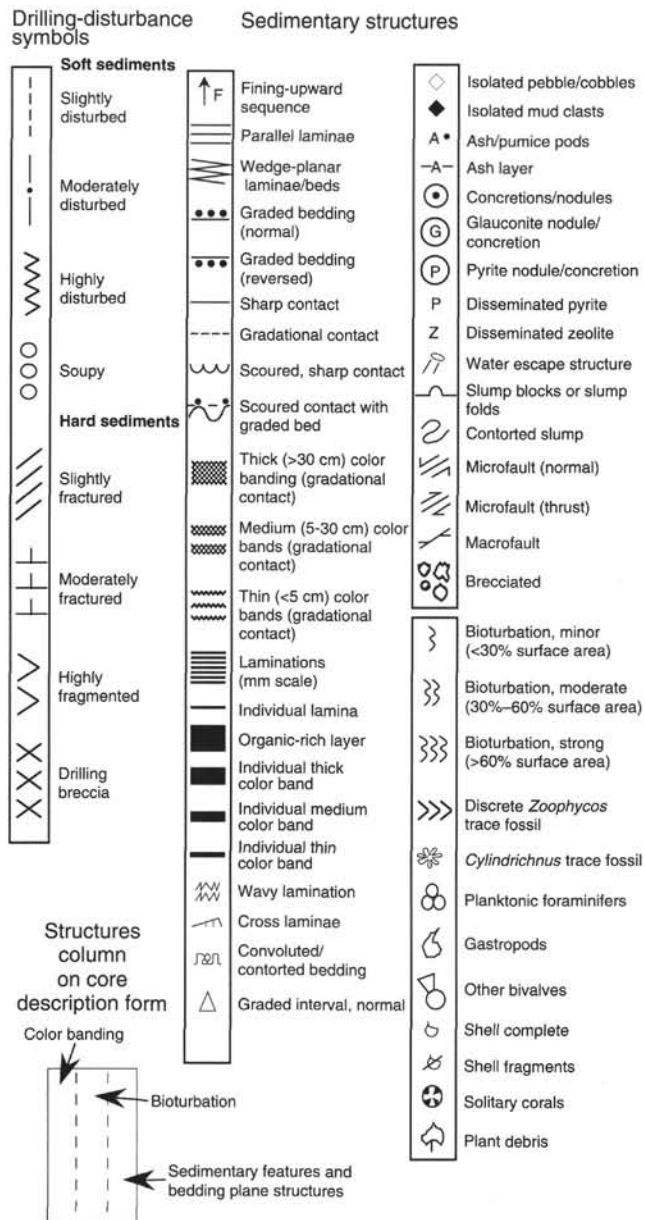
Drilling-disturbance
symbols

Sedimentary structures

Structures
column
on core
description form

Color banding

Bioturbation

Sedimentary features and
bedding plane structures

Figure 3. Symbols used for drilling disturbance and sedimentary structures
and components on the computer-generated core summaries. Layout of sym-
bol position in the "structures" column on core summaries.

Siliciclastic Sediments

For siliciclastic sediments, the principal name describes the tex-
ture and is assigned according to the following guidelines:

1. The Udden-Wentworth grain-size scale (Wentworth, 1922)
   defines grain-size ranges and names of the textural groups
   (gravel, sand, silt, and clay) and subgroups (fine sand, coarse
   silt, etc.) that are used as principal names of siliciclastic sedi-
   ment.
2. Principal names are listed in order of increasing abundance
   when two or more textural groups or subgroups are present in
   a siliciclastic sediment (Shepard, 1954; Fig. 5). For simplicity,
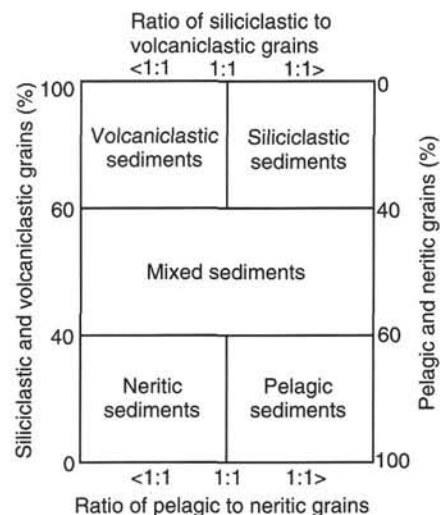

Figure 4. Diagram showing classes of granular sediment (modified from
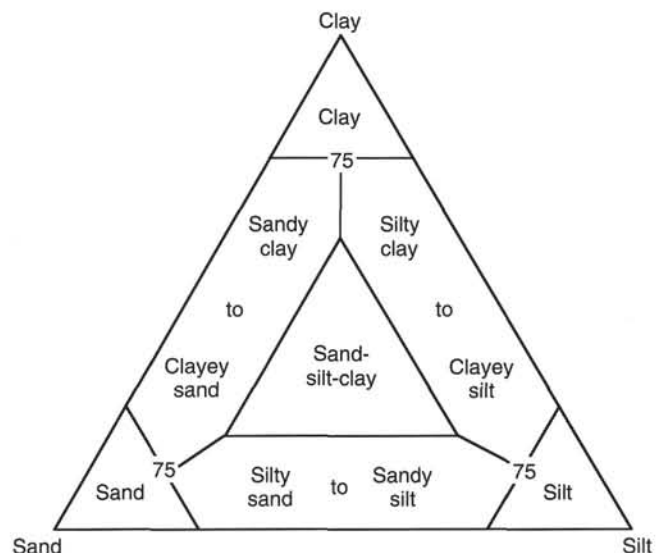Mazzullo et al., 1988).

Figure 5. Ternary diagram showing principal names for siliciclastic sedi-
ments (modified from Shepard, 1954).

we have grouped intermediate mixtures of the three textural
end members, sand, silt and clay, into four categories as shown
in Figure 5.
3. The suffix "stone" is affixed to the principal names sand, silt,
   and clay when a saw must be used to cut samples from the
   core. Conglomerate and breccia are used as principal names of
   lithified gravels with well-rounded and angular clasts, respec-
   tively.

Volcaniclastic Deposits

We slightly modified the classification of Mazzullo et al. (1988)
in regard to principal names of volcaniclastic deposits. Volcaniclastic
components have been subdivided into two groups (Fisher and
Schmincke, 1984): (1) pyroclastic fragments, which are particles ex-

pelled through volcanic vents, without reference to the causes of eruption or origin of the clasts (these fragments remain pyroclastic even if reworked), and (2) epiclastic fragments, which are fragments produced by the weathering, erosion, and transport of volcanic rocks. Epiclastic volcanic fragments are commonly associated with terrigenous components and are also commonly more altered and oxidized than pyroclastic debris. Deposits with a ratio of pyroclastic (ash) to epiclastic (terrigenous; sand/silt/gravel) material greater than 1:1 are classified according to the scheme outlined below.

The names and ranges of three textural (grain-size) groups for pyroclastic material from Fisher and Schmincke (1984) are used and slightly modified as follows:

1. *Pyroclastic breccia* (bombs of Schmid, 1981): clasts >64 mm diameter;
2. *Lapilli:* clasts from 64 to 2 mm diameter (lithified = *lapillistone*);
3. *Ash:* clasts <2 mm diameter (lithified = *tuff*).
   The ash component of the ODP scheme can be further divided into:
3a. *Coarse ash:* material ranging from 2- to 1/16-mm diameter (equivalent to sand in siliciclastic sediments). *Coarse tuff =* lithified coarse ash; and
3b. *Fine ash:* material <1/16-mm diameter (silt and clay size). *Fine tuff =* lithified fine ash.

Epiclastic sediment principal names are based on grain size using the same nomenclature as the classification for siliciclastic sediments:

1. *Volcanic breccia and gravel:* clasts >64 mm diameter;
2. *Lapilli:* clasts from 64 to 2 mm diameter (lithified = *lapillistone*);
3. *Volcanic sand:* clasts <2 mm diameter (lithified = *tuff*).

In addition, major modifiers (>30%) can be used to describe degree of lithification, grain fabric, grain shape, and sediment color. The principal modifiers typically used in the classification of volcaniclastic sediments include lithic, vitric, and crystal; modifiers are adopted here only for lithic components (e.g., basaltic lithic volcanic breccia).

Pelagic Sediments

For pelagic sediments, the principal name describes the composition and degree of lithification using the following terms:

1. *Ooze:* unlithified calcareous and/or siliceous pelagic sediments with ≥60% biogenic pelagic components;
2. *Chalk:* partially lithified ooze predominantly composed of calcareous pelagic grains;
3. *Limestone:* lithified ooze predominantly composed of calcareous pelagic grains;
4. *Radiolarite, diatomite,* and *spiculite:* partially lithified ooze predominantly composed of siliceous radiolarians, diatoms, and sponge spicules, respectively;
5. *Porcellanite:* a well-indurated rock with abundant authigenic silica but less hard, lustrous, or brittle than chert (in part, such rocks may represent mixed sedimentary rock);
6. *Chert:* vitreous or lustrous, conchoidally fractured, highly indurated rock composed predominantly of authigenic silica.

The principal name of neritic calcareous sediments describes the texture and fabric. The classification scheme outlined below is from Embry and Klovan (1971) after Dunham (1962; see lower left of Fig. 2). For neritic calcareous sediments the following terms apply:

1. *Mudstone:* mud-supported fabric with less than 10% grains, grains <2 mm in size;
2. *Wackestone:* mud-supported fabric with greater than 10% grains, grains <2 mm in size;
3. *Packstone:* grain-supported fabric with intergranular mud, grains <2 mm in size;
4. *Grainstone:* grain-supported fabric, no mud, grains <2 mm in size;
5. *Floatstone:* matrix-supported fabric, grains >2 mm in size;
6. *Rudstone:* grain-supported fabric, grains >2 mm in size;
7. *Boundstone:* components organically bound during deposition;
8. *Bafflestone:* formed by organisms that act as baffles;
9. *Bindstone:* formed by organisms that encrust and bind; and
10. *Framestone:* formed by organisms that build a rigid framework.

Mixed Sediments

Mixed sediments are described using major and minor modifiers indicating composition and texture. In mixtures of biogenic and non-biogenic material where neither component exceeds 60%, we have established a convention that the principal name will consist of two parts: (1) the name of the major fossil component(s), hyphenated, if necessary, with the most common fossil listed first, followed by (2) the textural name appropriate for the components (Fig. 5). A component with an abundance of 30%–60% qualifies for major modifier status; examples of major modifiers include nannofossil, foraminifer, diatom, and radiolarian. The general terms siliceous and calcareous are used when a mixture of calcareous or siliceous biogenic components forms the necessary 30%–60% of the sediment. If nannofossils form 30%–60% of a sediment, and the grain size of that sediment is predominantly clay, then the name is nannofossil clay. A component with an abundance of 10%–30% qualifies for minor modifier status and is hyphenated with the word "-rich". (Example: nannofossil-rich clay.) An unusual, important component that constitutes 5%–10% can be indicated with a minor modifier that consists of the name of the sediment followed by the word "with" followed by the component name. (Example: clay with nannofossils.)

Organic-Rich Layers

One major focus of Leg 161 was the identification and correlation of organic-rich sediments in the western Mediterranean Sea. The term "sapropel" has been used to describe marine sediments with high organic carbon content, but the lower limit of weight percent total organic carbon (TOC) that determines whether the term sapropel is used varies from 0.5% to 2.0% in the literature (see discussion in Hilgen [1991] and Kidd et al. [1978]). Organic-rich intervals can be tentatively identified in the core by their dark color and the presence of significant quantities of organic matter in smear slides of these intervals. However, quantitative TOC data, provided by shipboard geochemical analysis, are needed to confirm these intervals as true "sapropels" (note that the percent [volume] organic matter estimated from smear-slide analysis is often much greater [up to a factor of 7] than the measured TOC). Thus, because of the time lag between shipboard description and geochemical analysis of these intervals, we chose to call them "organic-rich intervals," rather than "sapropels." These intervals are marked with a characteristic lithologic symbol in the structure column of the VCDs, and are listed by interval individually in the VCD description section. Organic-rich layers are also classified as homogeneous, color-banded, or composite, based on

their appearance, in order to assist in correlation among holes at a given site.

X-Ray Diffraction

The bulk mineralogy of sediment samples was analyzed using standard X-ray diffraction techniques. Bulk samples were oven-dried or freeze-dried, ground to a fine powder with a mortar and pestle or ball mill, then packed into aluminum holders.

The shipboard Phillips X-ray diffractometer is equipped with a PW-1729 X-ray generator, PW-1710/00 diffraction control unit with a PW-1775 35-port automatic sample changer. Machine settings were as follows: generator = 40 kV and 35 mA; radiation = CuKα; focus = fine; divergence slit = automatic; receiving slit = 0.2 mm; step size = 0.01° 2θ; count time per step = 0.5 s; ratemeter time constant = 0.2 s; spinner = off; monochromator = on; scan = continuous; scanning range = 2°–70° 2θ.

Digital data were processed using a Phillips peak fitting program that subtracts background intensities and fits ideal curve shapes to individual peaks or ranges of peaks, as specified by the operator. Output of the processed digital data includes the angular position of each peak (°2θ), d-spacing (Å), peak width (Δ°2θ), intensity or height (counts per second above background), and peak area (integrated counts above background).

In addition to the routine identification of important minerals, we estimated relative abundances of total clay minerals, quartz, plagioclase, and calcite using a simultaneous linear equation algorithm that accounts for peak overlay (Karlak and Burnett, 1966; Wilkens et al., 1992). The quantification routine was calibrated using nine different mixtures of the four phases prepared by combining commercially available standard minerals. Diagnostic peak positions are shown in Table 1.

The relative abundances of the major minerals were normalized to 100%. Because of the presence of small quantities of crystalline minerals not included in our calculations, plus amorphous solids (volcanic glass, biogenic silica, organic matter, poorly formed clay crystallites, etc.), the relative abundances reported here may be significantly greater than the true absolute weight percentages. No attempt was made to quantify the weight percent of amorphous material.

BIOSTRATIGRAPHY

Initial biostratigraphic determinations for calcareous nannofossils, planktonic foraminifers, and benthic foraminifers were based on core-catcher assemblages. Additional samples were selected from sections as necessary in order to refine the biostratigraphic assignments.

For the Pliocene–Pleistocene planktonic foraminiferal biostratigraphy, the zonal scheme of Cita (1975) amended by Sprovieri (1992, 1993) was used. For the middle and upper Miocene, the biostratigraphic scheme of Iaccarino (1985) emended by Foresi et al. (in press) was followed. Whenever possible, a comparison with the standard zonation of Blow (1979) has been made. Nannofossil biostratigraphy was based on the standard zonation of Martini (1971).

Correlation between biostratigraphic zonations and the magnetic polarity reversal record, where available, are based on Cande and Kent (1995) and Shackleton et al. (1995). The zonal schemes used and the geomagnetic time scale are presented in Figures 6 through 8. Biochronology of the main calcareous nannofossil and planktonic foraminifer datums is given in Table 2. Some minor changes in the form of additional datums are discussed in the individual sections for particular fossil groups. Fossil abundance, preservation, and zone designations for each fossil group were documented using FossiList software.

Table 1. Diagnostic peak positions of minerals.

Mineral	Window (°2θ)	D-spacing (Å)
Calcite	29.25–29.60	3.05–3.01
Plagioclase	27.80–28.15	3.21–3.17
Quartz	20.80	4.26
Total clay minerals	19.7–19.9	4.50–4.46

Calcareous Nannofossils

Nannofossil assemblages were identified in slides (prepared by the settling method of de Kaenel and Villa [in press]) for each core-catcher sample using 3 × 1-in slides and 22 × 40 × 1.5-mm cover slips mounted with Norland Optical adhesive #61. Additional slides were prepared from intervals where lithologic changes and clasts were observed. The taxa identifications were performed on board using a Zeiss Axioscope under plane-polarized and cross-polarized light.

Abundance estimates of the nannofossil slides were made for areas of the slide without appreciable piling of specimens or other material. The estimates of nannofossils in each slide were made using a magnification of 1000×. The relative abundance of nannofossil species in a given sample was estimated using the following categories:

VA = very abundant: more than 100 specimens of a single species per field of view;
A = abundant: more than 10 specimens per field of view;
C = common: 1–10 specimens per field of view;
F = few: 1 specimen per 2–10 fields of view;
R = rare: 1 specimen per 11–100 fields of view;
VR = very rare: 1 specimen per 101–1000 fields of view;
B = barren: no indigenous calcareous nannofossils.

Calcareous nannofossils often show signs of both significant etching and overgrowth, when more dissolution-resistant forms add secondary calcite provided by dissolution-prone morphotypes. The following descriptive categories have been created to record the various states of preservation observed and followed the comments of Roth and Thierstein (1972).

G = Good: little or no evidence of dissolution and/or secondary overgrowth of calcite. Diagnostic characteristics are fully preserved and all specimens can be identified with certainty.
M–G = Moderate to Good: slight to moderate dissolution and/or overgrowth. The identification of some species is impaired.
M = Moderate: dissolution and/or secondary overgrowth partially alter primary morphological characteristics, but nearly all specimens can be identified at the species level.
P = Poor: severe dissolution, fragmentation, and/or secondary overgrowth with primary features largely destroyed. Many specimens cannot be identified at the species and/or generic level.

The calcareous nannofossil biozonation used for Leg 161 is that of Martini (1971), as modified by Varol (1989), by Rio et al. (1990), and by Young (1991) for the Miocene, Pliocene, and Pleistocene. The Mediterranean zonation from Theodoridis (1984) was followed for the upper Miocene to further subdivide the Messinian interval (Rotaria, Primus, and Pelagicus Subzones) (Figs. 6, 7). One of the modifications of Martini's zonation is to place the lower/upper Pliocene boundary at the last common occurrence (LCO) of *Reticulofenestra*
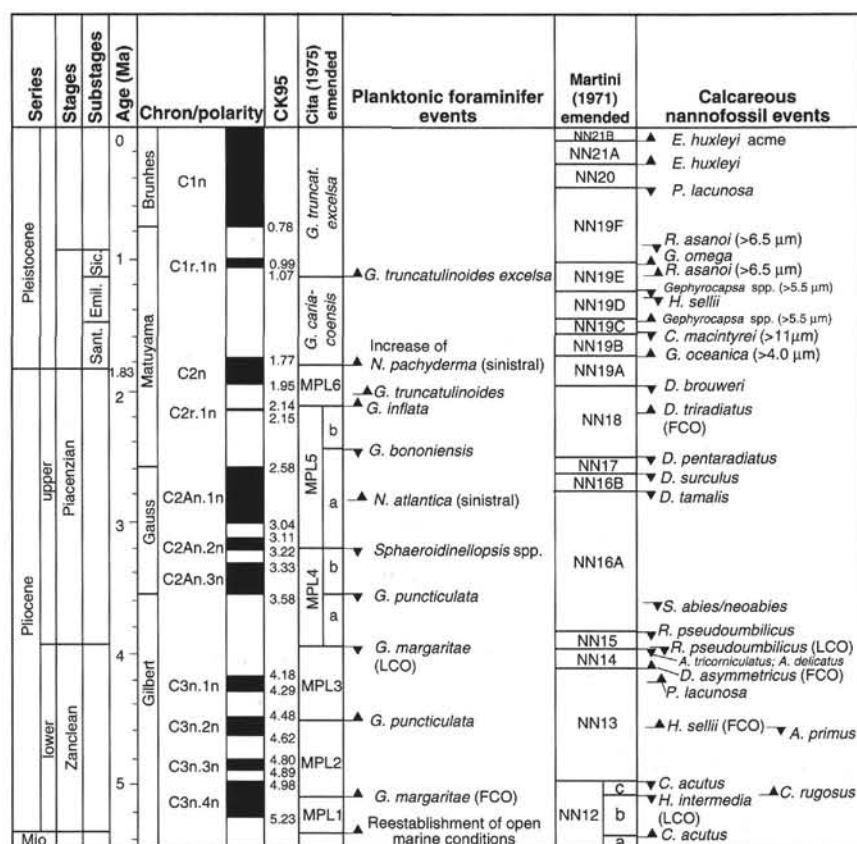
Figure 6 (chronostratigraphic chart):

Series	Stages	Substages	Age (Ma)	Chron/polarity	CK95	Cita (1975) emended	Planktonic foraminifer events	Martini (1971) emended	Calcareous nannofossil events
Pleistocene			0	Brunhes C1n		G. truncat. excelsa		NN21B / NN21A / NN20	▲ E. huxleyi acme / ▲ E. huxleyi / ▼ P. lacunosa
		Sic.			0.78			NN19F	▼ R. asanoi (>6.5 µm)
		Emil.	1	C1r.1n	0.99 / 1.07		▲ G. truncatulinoides excelsa	NN19E	▲ G. omega / ▲ R. asanoi (>6.5 µm) / ▼ Gephyrocapsa spp. (>5.5 µm)
		Sant.		Matuyama		G. caria-coensis		NN19D	▼ H. sellii
			1.83	C2n	1.77		Increase of N. pachyderma (sinistral)	NN19C / NN19B / NN19A	▲ Gephyrocapsa spp. (>5.5 µm) / ▼ C. macintyrei (>11µm) / ▲ G. oceanica (>4.0 µm)
			2	C2r.1n	1.95 / 2.14 / 2.15	MPL6	▲ G. truncatulinoides / ▲ G. inflata	NN18	▼ D. brouweri / ▲ D. triradiatus (FCO)
upper	Piacenzian				2.58	MPL5 b	▼ G. bononiensis	NN17	▼ D. pentaradiatus
				Gauss C2An.1n		a	▲ N. atlantica (sinistral)	NN16B	▼ D. surculus / ▼ D. tamalis
			3	C2An.2n	3.04 / 3.11 / 3.22	MPL4 b	▼ Sphaeroidinellopsis spp.	NN16A	
				C2An.3n	3.33 / 3.58	a	▼ G. puncticulata		▼ S. abies/neoabies / ▼ R. pseudoumbilicus
Pliocene			4	Gilbert C3n.1n	4.18 / 4.29	MPL3	▲ G. margaritae (LCO)	NN15 / NN14	▼ R. pseudoumbilicus (LCO) / ▲ A. tricorniculatus; A. delicatus / ▲ D. asymmetricus (FCO) / P. lacunosa
				C3n.2n	4.48 / 4.62		▲ G. puncticulata	NN13	▲ H. sellii (FCO) / ▼ A. primus
lower	Zanclean		5	C3n.3n	4.80 / 4.89 / 4.98	MPL2			
				C3n.4n		MPL1	▲ G. margaritae (FCO)	NN12 c / b / a	▼ C. acutus / ▼ H. intermedia (LCO) / ▲ C. rugosus / ▲ C. acutus
Mio					5.23		▲ Reestablishment of open marine conditions		

Figure 6. Pliocene and Pleistocene chronostratigraphic units correlated with planktonic foraminiferal and nannofossil zonations and with the geomagnetic polarity time scale of Cande and Kent (1995). Sant. = Santernian; Emil. = Emilian; Sic. = Sicilian.

pseudoumbilicus (>7.0 µm). Therefore, this boundary is placed between the calcareous nannofossil zones NN14/NN15. Tops of Subzones NN12a, NN12b, and NN12c are defined respectively by the first occurrence of *Ceratolithus acutus,* by the last consistent occurrence of *Helicosphaera intermedia,* and by the last occurrence of *Ceratolithus acutus.*

Planktonic Foraminifers

Some emendations in the Miocene zonal scheme of Iaccarino (1985) are introduced. (1) *G. conomiozea* Zone is defined by the first regular occurrence (FRO) of *G. conomiozea* gr. which includes the ancestor form *G. miotumida* (in the sense of Krijgsman et al., in press). (2) *N. acostaensis* Zone is defined by the first common occurrence (FCO) of the nominal taxon, which occurs immediately below the last occurrence (LO) of *G. siakensis* (Foresi et al., in press).

Taxonomic identifications follow the scheme proposed by Hemleben et al. (1989) for recent taxa.

Approximately 10 cm³ of sediment was disaggregated in water or hydrogen peroxide and washed under running water through a 63-µm mesh sieve. Dried residues were then processed through 63–125-µm and >125-µm sieves. The dried samples were examined under a binocular microscope.

The following categories are used to indicate abundance:

A = abundant: more than 50 specimens/picking tray;
C = common: more than 10 specimens/picking tray;
F = few: 5–10 specimens/picking tray;
R = rare: 1–2 specimens/picking tray;
B = barren: no planktonic foraminifers.

The state of preservation of planktonic foraminifers is described as follows:

G = good: little or no fragmentation, overgrowth, and/or dissolution;
M = moderate: some signs of fragmentation, overgrowth, and/or dissolution;
P = poor: severe fragmentation, heavy overgrowth, and/or dissolution.

Benthic Foraminifers

Benthic foraminiferal assemblages are a primary source of paleobathymetric information. During shipboard examination, assemblage information was utilized as much as possible. Benthic foraminifers were analyzed in the same samples used for planktonic assemblages. Bathymetric zonations follow that discussed by Wright (1978) and established during Leg 42 and that of Hasegawa et al. (1990) used in Leg 107.

The categories used for the abundance and preservation are the same as those for planktonic foraminifers.

Paleoenvironmental Interpretation

In addition to biostratigraphic data, microfossils were used for paleoenvironmental interpretation. Where applicable, relative paleodepth evaluations were made using both planktonic and benthic foraminifers.

Presence, abundance, and species diversity of all the microfossils identified during Leg 161 will also allow the paleoclimatic interpretation of the Mediterranean Sea through time.
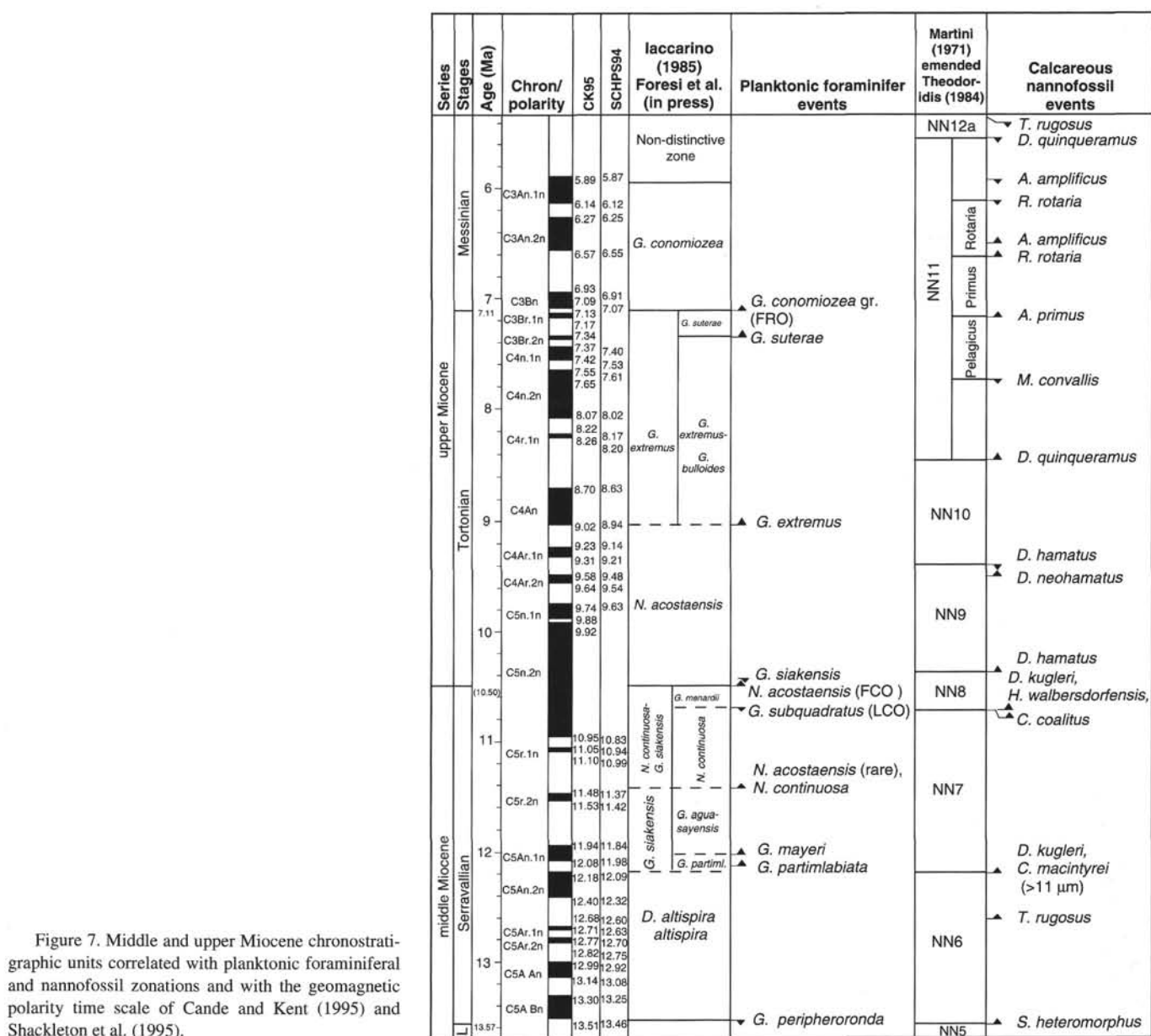
Figure 7. Middle and upper Miocene chronostratigraphic units correlated with planktonic foraminiferal and nannofossil zonations and with the geomagnetic polarity time scale of Cande and Kent (1995) and Shackleton et al. (1995).

PALEOMAGNETISM

Paleomagnetic studies aboard the *JOIDES Resolution* during Leg 161 included routine pass-through measurements and alternating field (AF) demagnetization of natural remanent magnetization (NRM) of the archive half of all cores. Progressive AF demagnetization was applied to some of the archive halves and discrete samples for the higher level of AF demagnetization. Thermal demagnetization was also performed on a limited number of discrete samples.

Rock-magnetic studies investigated mineralogy, abundance, and grain size of magnetic minerals in the cores. Low-field magnetic susceptibility (K) was measured for whole-round cores on the multisensor track (MST) and for discrete samples. Anisotropy of magnetic susceptibility (AMS) was also determined for discrete samples to study magnetic fabric and rock magnetism.

Core Orientation and Discrete Samples

Core orientation was performed at selected advanced hydraulic piston cored (APC) holes, starting with the third core, using the Tensor tool (Shipboard Scientific Party, 1993). Several types of discrete samples were taken for shipboard and personal post-cruise studies including standard ODP paleomagnetic cubes (7 cm³) and 1 cm³ cubes, which are used for small-volume or high-resolution sampling of discrete layers like sapropels. The newly designed, more symmetrical 7-cm³ Kyoto type cube, which fits the standard paleomagnetic sample

Figure 8. Correlation between the standard chronostratigraphic units of the Pliocene–Pleistocene with the updated chronostratigraphic stages (Rio et al., 1994).

Table 2. Ages of main planktonic foraminifer and calcareous nannofossil events used in Leg 161.

Event	Age (Ma)
FO *Emiliania huxleyi > Gephyrocapsa* spp.	0.085
FO *Emiliania huxleyi*	0.26
LO *Pseudoemiliania lacunosa*	0.46
LO *Reticulofenestra asanoi* (= Ret. sp. A >6.5 µm)	(0.93)
FO *Gephyrocapsa omega* > 4.0 µm	1.02
FO *Reticulofenestra asanoi* (= Ret. sp. A >6.5 µm)	(1.10)
LO *Gephyrocapsa* spp. >5.5 µm	1.24
LO *Helicosphaera sellii*	(1.27)
FO *Gephyrocapsa* spp. >5.5 µm	1.44
LO *Calcidiscus macintyrei* (cir., >11 µm)	1.58
FO *Gephyrocapsa oceanica* >4.0 µm	(1.75)
FCO *Neogloboquadrina pachyderma* left	1.79
LO *Discoaster brouweri*	1.96
FO *Globorotalia inflata*	2.13
FCO *Discoaster triradiatus*	(2.15)
LO *Globorotalia bononiensis*	2.45
LO *Discoaster pentaradiatus*	2.52
LO *Discoaster surculus*	2.63
LO *Discoaster tamalis*	2.78
LO *Sphaeroidinellopsis* spp.	3.22
LO *Globorotalia puncticulata*	3.57
LO *Sphenolithus abies/neoabies*	3.66
FCO *Discoaster tamalis*	3.80
LO *Reticulofenestra pseudoumbilicus* (>7 µm)	3.82
LCO *Globorotalia margaritae*	3.94
LCO *Reticulofenestra pseudoumbilicus* (>7 µm)	(3.94)
LO *Amaurolithus tricorniculatus, A. delicatus*	(3.95)
FCO *Discoaster asymmetricus*	4.13
FO *Pseudoemiliania lacunosa*	4.20
FcO *H. sellii*	4.52
FO *Globorotalia puncticulata*	4.52
LO *Amauroliithus primus*	4.56
LO *H. intermedia*	4.67
LO *Ceratolithus acutus*	4.99
FO *Ceratolithus rugosus*	5.07
LcO *H. intermedia*	5.07
FCO *Globorotalia margaritae*	5.10
Re-establishment open marine conditions	5.33
FO *Ceratolithus acutus*	5.34
LO *Triquetrorhabdulus rugosus*	5.35
LO *Discoaster quinqueramus*	5.55
LO *Amaurolithus amplificus*	5.93
LO *Reticulofenestra rotaria*	6.12
FO *Amaurolithus amplificus*	6.50
FO *Reticulofenestra rotaria*	6.62
Top absence interval of *R. pseudoumbilicus* (>7 µm)	6.76
FRO *Globorotalia conomiozea* gr.	7.11
FO *Amaurolithus primus*	7.17
FO *Globorotalia suterae*	7.35
LO *Minylitha convallis*	7.73
FCO *Discoaster surculus*	7.80
FO *Discoaster berggrenii*	8.45
FO *Discoaster pentaradiatus*	8.55
Base absence interval of *R. pseudoumbilicus* (>7 µm)	8.71
FO *Minylitha convallis*	9.37
LO *Discoaster hamatus*	9.40
LO *Discoaster neohamatus*	9.52
FO *Discoaster neohamatus*	9.60
FO *Discoaster hamatus*	10.38
LO *Discoaster kugleri*	10.72
LO *Helicosphaera walbersdorfensis*	(10.72)
FO *Catinaster coalitus*	10.73
LCO *Discoaster kugleri*	11.34
FCO *Discoaster kugleri*	11.74
LO *Coronocyclus nitescens*	12.12
FO *Calcidiscus macintyrei* (>11 µm)	12.20
FO *Discoaster kugleri*	12.20
FO *Triquetrorhabdulus rugosus*	12.62
LCO *Cyclicargolithus floridanus*	13.19
LO *Sphenolithus heteromorphus*	13.57

Notes: FO = first occurrence, LO = last occurrence, FCO = first common occurrence, LCO = last common occurrence, FRO = first regular occurrence, FcO = first consistent occurrence, LcO = last consistent occurrence. Calcareous nannofossil ages are from Shackleton et al. (1995). Ages in parentheses are from Sprovieri (1993) or estimated. Foraminifer ages are from Sprovieri (1993) and Krijgsman et al. (in press).

holder (1-in diameter), was also used. We followed the sample orientation method of previous cruises (e.g., Shipboard Scientific Party, 1991).

NRM Direction and Intensity

NRM direction and intensity along the cores were measured on vertically split half-cores (archive half). A cryogenic magnetometer (2G SRM 760-R) was used for both pass-through measurements of archive halves (CryoSect mode) and for some discrete samples (CryoCube or CryoSpin modes). AF demagnetization was routinely performed at 15 or 25 mT, according to the intensity of NRM, with a co-axial degausser. Progressive AF demagnetization up to 25 or 30 mT was performed on archive halves as time permitted. In addition to the pass-through measurements, discrete samples were demagnetized to isolate a characteristic remanent component by applying AF up to 100 mT (peak to peak value). A single axis AF demagnetizer (Schonstedt GSD-1) was used for the higher level AF demagnetization. Most of the discrete samples were measured with a spinner magnetometer (Molspin). Thermal demagnetization was applied to erase stable secondary overprinting by using a Schonstedt TSD-1 demagnetizer.

Magnetic Overprint

We have encountered several types of overprint during this cruise. Steep downward overprints (positive inclination more than 80°) were ubiquitous at all sites. These overprints were removed by the application of AF demagnetization at 5–10 mT. It should be noted that before Leg 152, the steep overprint was always in an upward direction.

A second type of overprint was observed as a clustered declination at around 0° for the archive half and 180° for the working half, parallel to the X-axis of the core coordinate. This type of overprint was first reported by Leg 154 paleomagnetists (Shipboard Scientific

Party, 1995c) and also reported at Leg 159 (Shipboard Scientific Party, 1996). Leg 154 paleomagnetists found that the clustered declination around 0° was caused by a radially concentric remagnetization of whole core and called this magnetization pervasive radial remagnetization (PRR; Fig. 9A). After various tests, they interpreted PRR was caused by a cutting shoe. During this cruise, we observed PRR at all sites; it was most pronounced at Sites 974 and 975. We took several 2-cm-thick one-quarter-core samples at Hole 974C and subdivided these segments into four to five small subsamples. The NRM direction of most subsamples points in a steep and concentric direction (Fig. 9B, C). We also found declinations clustered around 20° in XCB archive halves, even in those that had been strongly biscuitted (see "Paleomagnetism" section, "Site 974" chapter, this volume).

It is difficult to give a simple interpretation for the clustered declinations observed in APC and XCB. One plausible explanation is a remagnetization attributable to deformation caused by coring. Almost all APC and XCB sediments show strong deformation at the edge. This deformation is commonly observed in APC cores where the outer parts of the core are dragged down by the friction of the core liner. This rotates and reorients the remanent vector of the core edges. As shown by Leg 134 paleomagnetists (Shipboard Scientific Party, 1992), edges of core samples are always strongly overprinted, and edge deformation may produce symmetrical remagnetization, similar to that observed in PRR. This, however, cannot produce asymmetric directions, as observed in the XCB cores. More detailed observations and experimental studies need to be made to understand PRR and related phenomena.
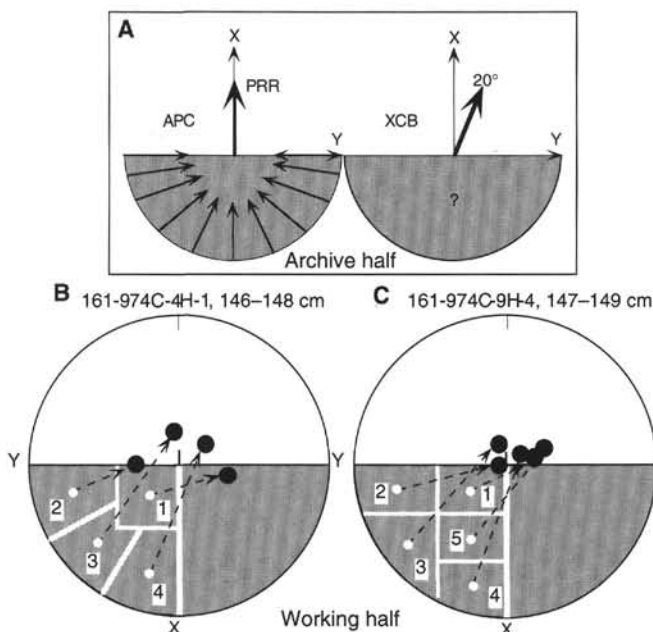

Figure 9. **A.** Clustered declinations in APC (left) and XCB (right). APC declinations can be explained by a radially concentric vector sum proposed as PRR (see text). No interpretation is proposed for XCB data. **B, C.** NRM directions from various positions of a half (one-quarter core) segment of the working half from Sample 161-974C-4H-1, 146–148 cm (B) and 9H-4, 147–149 cm (C). Pieces of pie-shaped, 2-cm-thick segments were taken at four horizons from Hole 974C. Each segment was subdivided into four or five small pieces, and the NRM direction was measured. The shape of each small portion is indicated by the white lines. NRM directions were plotted on an equal area projection. The projection coordinate is rotated 180° from the ordinal position. NRM directions are mostly concentric, and there is no significant change by AF demagnetization above MDF.

A third type of overprint was found at Site 979. After AF demagnetization, declinations clustered around 200° but were rather scattered before the demagnetization (see "Paleomagnetism" section, "Site 979" chapter, this volume). Because this was only found after the demagnetization at 15 mT, we thought this might be artificially remagnetized, possibly an acquisition of anhysterectic remanent magnetization (ARM) caused by the cryogenic magnetometer degausser. We also observed acquisition of spurious ARM several times, particularly in demagnetizing discrete samples in CryoCube mode. The spurious ARM is parallel with the X axis, suggesting imbalance between X and Y degaussing coils and/or related electronic circuits.

Magnetostratigraphy

Based on stable inclination data, correlation with the Geomagnetic Polarity Time Scale (GPTS; Cande and Kent, 1995) was attempted in conjunction with biostratigraphic data at Site 978 (see also "Biostratigraphy" section, this chapter).

Rock-Magnetic Study

Rock-magnetic studies are indispensable to understand remanent or induced magnetizations. To investigate mineralogy, abundance, and grain size of the dominant magnetic minerals in core samples, we made various rock-magnetic studies on discrete samples. Anhysteretic remanent magnetization (ARM) was imparted at 100 mT AF (peak), biased by a small DC field (79.6 A/m) using a DTECH ARM coil coaxial with an AF demagnetizer (GSD-1). ARM is carried by relatively fine grains among magnetic minerals and is thought to represent carriers of stable NRM in most cases. ARM intensity was expressed as a susceptibility of ARM (K_{arm}) for normalization, divided by the strength of the biasing DC field.

Isothermal remanent magnetization (IRM) was imparted by using an impulse magnetizer (ASC IM-10). Saturated IRM (SIRM) was used to evaluate total magnetization. Backfield IRM (imparted in an antiparallel direction to SIRM) at various intensities was used. For instance, $S_{-0.3T} = \{(-IRM_{-0.3T}/SIRM) + 1\}/2$ is thought to express the ratio of less coercive magnetic minerals (mostly magnetite or titanomagnetite in marine sediment) to highly coercive antiferromagnetic minerals such as hematite (Bloemendal et al., 1992). We also applied 0.1 T backfield as necessary to evaluate less coercive magnetic minerals. Median destructive field (MDF) of NRM and ARM, which is the demagnetizing field required to reduce the initial magnetization by half, was sometimes obtained to estimate dominant magnetic grain size (modified Lowrie-Fuller test; Johnson et al., 1975). Thermal demagnetization of composite IRMs imparted along the X, Y, and Z axes of a sample gives crucial information about magnetic mineralogy (Lowrie, 1990) and was applied to identify magnetic minerals in the hard-rock samples recovered at Hole 976B.

Low-field (initial) susceptibility (K) was used to evaluate total magnetic (including paramagnetic and diamagnetic) response. On the MST, K was measured every 3 cm for all sections, using a Bartington M.S.1 and M.S.1/CX 80 whole sensor at 0.465 kHz. Conversion of volume susceptibility into SI volume susceptibility units was done by multiplying raw data by 0.63×10^{-5} (Shipboard Scientific Party, 1993). Low-field susceptibility of discrete samples was measured by using a Bartington M.S.2 susceptometer and M.S.1.B sensor at 0.46 kHz (K_{low}) and 4.6 kHz (K_{high}). Frequency dependence of susceptibility, $F_d (\%) = 100 \times (K_{low} - K_{high})/K_{low}$, were measured to estimate contribution of superparamagnetic contamination (Bloemendal et al., 1985). Measurements of K_{high}, however, were sometimes unstable and gave unusually high F_d values (>20%) or negative values. A Geofyzika Brno KLY-2 susceptibility bridge (Kappabridge) was also used to measure low-field susceptibility (at 0.92 kHz) of discrete samples. We compared K value on several tens of discrete samples
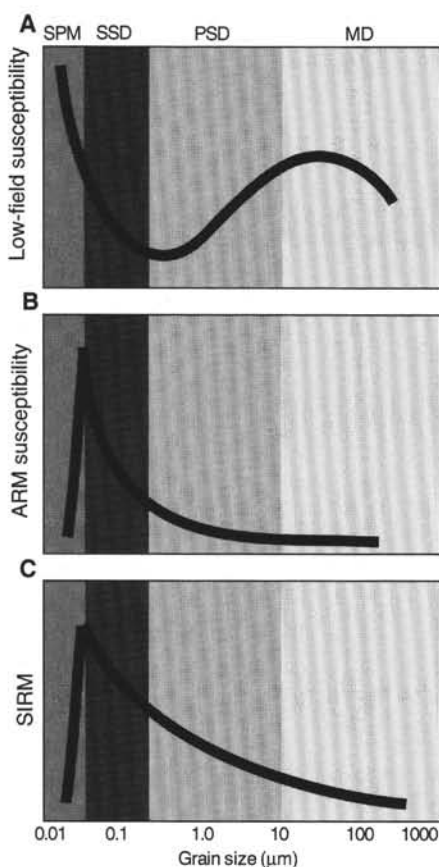
Figure 10. Size dependence of rock-magnetic parameters: low-field suscepti-bility (**A**); susceptibility of anhysteretic remanent magnetization (**B**); and sat-urated isothermal remanent magnetization (**C**). The curves are determined for sized pure magnetite; SPM (superparamagnetic grains), SSD (stable sin-gle domain), PSD (pseudo-single domain), and MD (multidomain). (Simpli-fied after Maher, 1988.)

by using the Bartington and Kappabridge susceptometers and found an almost perfect linear relationship between the two susceptometers. Good linearity between MST susceptibility data and discrete data were also confirmed (see also "Paleomagnetism" section, "Site 976" chapter, this volume).

General features of grain-size dependence of rock-magnetic pa-rameters are shown in Figure 10. These were obtained only for pure-sized magnetite (Maher, 1988) and thus cannot be simply assumed to be applicable to naturally occurring minerals. But comparing these size-diagnostic parameters will help to understand paleoenvironmen-tal change in terms of rock magnetism (e.g., Bloemendal et al., 1992).

Anisotropy of Magnetic Susceptibility (AMS)

The second-rank tensor derived from AMS measurements pro-vides the three-dimensional preferred orientation of grains (magnetic fabric). In general, magnetic fabric is dependent on the deformation history of the sediment (e.g., sedimentation, diagenetic compaction, extension, compression). It is particularly sensitive to disturbance and compaction. This information is important to identify spurious magnetizations caused by biogenic reworking or inclination errors in the NRM due to strong compaction.
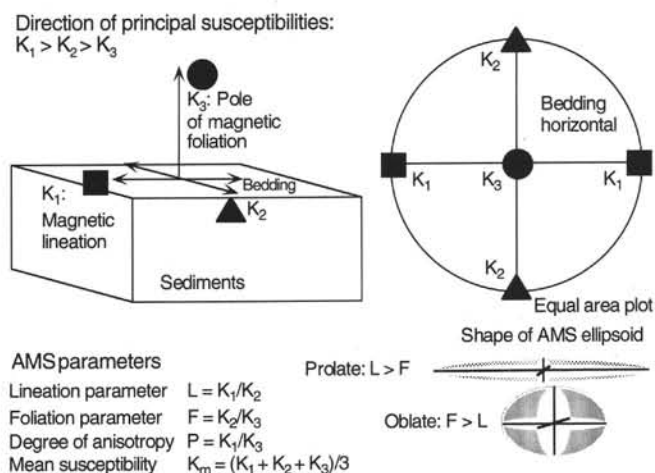

Figure 11. AMS axis and anisotropy parameters of the magnetic fabric. K_3 is usually perpendicular to the bedding in sediments.

We used standard parameters as described in Ellwood et al. (1988) and plotted eigenvalues $K_1 > K_2 > K_3$ on an equal area plot (Fig. 11). In sediments, K_3 (pole of magnetic foliation) is expected to be perpendicular to the bedding plane, whereas K_1 (magnetic linea-tion) could, in certain circumstances, be parallel to a sedimentary or tectonic lineation (Hrouda, 1982). We also used the following AMS parameters:

1. mean susceptibility, K_m, where $K_m = (K_1 + K_2 + K_3)/3$;
2. lineation parameter, L, where $L = K_1/K_2$, measures the linear preferred orientation ($L = 1$, pure oblate anisotropy);
3. foliation parameter, F, where $F = K_2/K_3$, which measures the oblateness of the ellipsoid (e.g., $L > F$ [$L < F$] indicates that the ellipsoid is prolate [oblate]); and
4. degree of anisotropy, P, where $P = K_1/K_3$, which measures semi-quantitatively the degree of deformation. In certain cas-es, a significant relationship between P and finite deformation is observed (Borradaile, 1988).

AMS measurements were performed using a Kappabridge, which has the capability to measure susceptibilities as low as 5×10^{-8} SI, with an accuracy of about 0.1%. Because of the magnetic noise on the ship, AMS measurements in sediments with susceptibilities between 5×10^{-4} and 10^{-6} SI and a degree of anisotropy $P < 1.1$ were difficult to obtain. This accuracy is enough to isolate the pole of magnetic fo-liation (K_3) but not the magnetic lineation (K_1).

COMPOSITE DEPTHS

Composite Section Development

The paleoceanographic objectives of Leg 161 required recovery of a continuous section of the sedimentary sequence. Drilling multi-ple holes at each site, with coring intervals offset in depth, helped to ensure that intervals missing within a single hole were recovered in an adjacent hole. Developing composite depth sections at the multi-ple-cored sites achieved the necessary continuity in the recovered sedimentary sequence. In this section we describe the methods used to produce composite sections. These methods are similar to those used to construct composite depth sections during Leg 138 (Hagel-berg et al., 1992), Leg 154 (Shipboard Scientific Party, 1995a), and Leg 160 (Shipboard Scientific Party, in press).

At each site, high-resolution measurements of magnetic susceptibility (3 cm), GRAPE wet-bulk density (2 cm), natural gamma radiation (15 cm), and *P*-wave velocity (10 cm) were made on whole-round core sections using the MultiSensor Track (MST). In addition, measurements of visible percent color reflectance were made every 2 cm on the split cores. Using GRAPE wet-bulk density, magnetic susceptibility, and 550 nm color reflectance as the primary correlation parameters, distinct intervals in each hole were correlated between the holes to provide verification of the extent of recovery of the sedimentary sequence.

Correlative features were aligned by adjusting the meters below seafloor (mbsf) depths (derived from drill pipe measurements) on a core-by-core basis. Cores were shifted as a unit; no depths were adjusted within a single core. The resulting adjusted depth scale is termed meters composite depth (mcd). The correlation process was iterative. Records of a single physical parameter were moved along a depth scale, core by core, as correlations between holes were made. The amount of adjustment necessary to optimize the correlation among multiple holes was recorded for each core of each hole. Where the amount of offset necessary to align features was ambiguous or uncertain, or where multiple hole data were unavailable, depth adjustments were carried down from the core above. At a given level, the total amount of offset between mbsf depth and mcd is equal to the cumulative offsets of the overlying cores. When complete, confirmation of the composite depth section was provided by comparison with lithologic observations of distinctive markers such as organic-rich layers or ash layers from multiple holes.

The composite depth section for each site is presented in tabular format. A portion of the composite depth table for Site 974 is given as an example in Table 3. For each core, the last two columns list the depth offset applied to mbsf and mcd. Adding the amount of offset to mbsf depth of a measurement taken in a particular core, the equivalent mcd is obtained.

After composite depth construction, a single spliced record, representative of the multiple cored sedimentary sequence at each site, was assembled. Because missing or duplicated sections of the sedimentary sequence in a single hole could be identified, it was possible to patch in missing intervals with data from adjacent holes or cut out duplicated sections. There may be stretching and/or compression of core relative to the same stratigraphic interval in adjacent holes. Thus, the precise length of the spliced section depends on which intervals of core are selected to assemble it. In particular, APC core tops were generally expanded relative to equivalent intervals located within the middle of the core in adjacent holes; the bases of cores were relatively compressed.

Splices were made at the same mcd level from core to core, assuring that mcd and spliced section depths are identical. Tables that give the tie points for the spliced record construction are given in each site chapter. An example is presented as Table 4. A significant advantage of the spliced record is that it provides a single complete and continuous sequence. This single record is ideally suited to serve as a sampling scheme for high-resolution stratigraphy and paleoceanographic studies.

METAMORPHIC AND IGNEOUS PETROLOGY

Core Curation and Shipboard Sampling

Metamorphic and igneous rock cores are usually broken into a series of disconnected fragments that have rotated with respect to one another about vertical axes. The first task of the shipboard structural geologist or petrologist is to prepare the core for splitting. Fragments that can be fitted together with confidence are grouped, and each fragment or assembled group of fragments is referred to as a "piece" and assigned a number. The pieces are numbered sequentially from

Table 3. Partial composite depth table from Site 974.

Hole	Core, section	Depth (mbsf)	Offset (m)	Depth (mcd)
974A	1H	5.00	0.66	5.66
974B	1H	0.00	0.00	0.00
974B	2H	6.50	1.10	7.60
974B	3H	16.00	1.38	17.38
974B	4H	25.50	1.58	27.08
974B	5H	35.00	2.50	37.50
974B	6H	44.50	3.34	47.84
974B	7H	54.00	4.53	58.53

Note: Depth (mbsf) + offset (m) = depth (mcd).

the top of each core section and labeled. Broken core fragments that can be fitted together into larger pieces are lettered consecutively from the top down (e.g., 1A, 1B, 1C, etc.). Plastic spacers are placed between pieces with different numbers. If it is evident that an individual piece or fragment has not rotated about a horizontal axis during drilling, an arrow is added to the label pointing to the top of the section. The core is then split with a diamond saw into archive and working halves so that the internal structure is best revealed. The core may be split parallel to a stretching lineation, parallel to the dip direction, or normally to fold axes, depending on which is most appropriate to the particular piece. As far as possible, they are split to allow important features and structures to be represented in both the working and archive samples. The way the core is split may result in an artificial grouping of structural data when plotted in core coordinates. This does not affect the possibility of reorienting the structures into geographic coordinates using Formation MicroScanner logging data.

Small quantities of vein and vesicle fillings are sampled from the working half for X-ray diffraction analysis to confirm mineral identity. Each lithologic unit of the working half of the core is sampled (where recovery permits) for shipboard studies. Shipboard samples and studies are indicated in the column headed "shipboard studies," using the following notation: XRD = X-ray diffraction analysis; XRF = X-ray fluorescence analysis; TSB = petrographic thin section; PP = physical properties analysis; and PM = paleomagnetic analysis. Where feasible, cubes or minicores for physical properties measurements are taken immediately adjacent to samples used for chemical analyses and thin sections.

Core Description

The archive half of the core is described on a paper visual core description (VCD) form and is photographed before storage. For the purposes of description, the core is subdivided into lithologic units on the basis of changes in texture, grain size, mineral occurrence and abundance, and rock composition. The following information is recorded in the database system:

A. The leg, site, hole, core number, core type, and section number, and who described the core;
B. The piece number or numbers (if there is more than one consecutive piece of the same rock type) and the rock type;
C. The color of the dry rock, the grain size, and any variations in grain size;
D. The mineral phases visible with a hand lens and their distribution within the unit, including porphyroblastic minerals with their size and textural relationships, and accessory, relict, or alteration minerals, with a note as to their position in the piece;
E. The presence and character of deformational fabrics and small-scale structures. The orientation of foliations and lineations in deformed rocks are measured, and visible microstructures (e.g., microfolds, shear bands, asymmetric porphyroclast sys-

Table 4. Partial splice table from Site 974.

Hole	Core, section, interval (cm)	Depth (mbsf)	Depth (mcd)		Hole	Core, section, interval (cm)	Depth (mbsf)	Depth (mcd)
974B	1H-4, 52	5.02	5.02	tie to	974D	2H-2, 40	3.40	5.05
974D	2H-6, 139	10.09	11.74	tie to	974B	2H-3, 115	10.65	11.75
974B	2H-6, 79	14.79	15.89	tie to	974D	3H-2, 4	12.54	15.90
974D	3H-6, 43	18.93	22.29	tie to	974B	3H-4, 40	20.90	22.28
974B	3H-6, 85	24.35	25.73	tie to	974D	4H-1, 118	21.68	25.73
974D	4H-5, 112	27.62	31.67	tie to	974B	4H-4, 10	30.10	31.68
974B	4H-6, 67	33.67	35.25	tie to	974D	5H-1, 58	30.58	35.24
974D	5H-5, 7	36.07	40.73	tie to	974B	5H-3, 22	38.22	40.72

tems) are noted (see "Structural Geology" section, this chapter);

F. The presence of veins and fractures, including their abundance, width, mineral fillings or coatings, relationship to the main foliation, and associated wall rock alteration. The orientation of veins and fractures with respect to the core axis is measured with a protractor (see "Structural Geology" section, this chapter). The relationship of the alteration and vein-filling minerals with respect to veins and fractures is also noted;

H. In igneous rocks, the groundmass texture: glassy, fine grained (<1 mm), medium grained (1–5 mm), or coarse grained (>5 mm);

I. The abundance, distribution, size, shape, and infilling material of vesicles in volcanic rocks (including the proportion of vesicles that are filled by alteration minerals);

J. The structure of a volcanic flow; whether it is massive, pillowed, thin or sheetlike, brecciated or a hyaloclastite.

Petrographic Descriptions of Metamorphic Rocks

Thin sections of metamorphic rocks are examined (1) to complement and refine the hand-specimen observations, (2) to help with the determination of the rock type, (3) to investigate the nature of the ductile deformational fabrics in more detail, (4) to determine time relationships between different deformational features, (5) to provide kinematic information, and (6) to determine the relationships between deformational events and the growth and alteration of metamorphic minerals.

Thin sections are oriented with respect to the core coordinates. They are cut either parallel to the core axis or in an appropriate orientation to study the structural features. This is likely to be at right angles to foliation or layering, and either parallel to a stretching lineation, or at right angles to fold or crenulation hinges.

Thin sections are described using the same terminology as is used for the core descriptions. Special terminology used in the description of migmatite rocks is summarized in Table 5. The percentages and textural descriptions of individual phases are reported using a database. The relationships between mineral growth and deformational phases are noted, and microscale features indicating the sequence of deformational events, the mechanism of deformation, and the kinematics of the deformation are recorded. Thin-section descriptions are included in the site summary appendices. A table summarizing the thin section data is provided for each site.

Petrographic Descriptions of Igneous Rocks

The texture of igneous rocks represents the geometrical relationships between the main component crystals. Absolute and relative sizes of crystals, crystal shapes, and arrangement of crystals are the main properties of texture. The texture is classified using the scheme laid out in Table 6. Rock names are assigned using triangular diagrams based on the primary minerals plagioclase, alkali feldspar, and quartz (Shelley, 1983; Fig. 12). Genetically significant accessory

Table 5. Textural terms for gneissic and migmatitic rocks.

I. Gneissic rocks
   a. Layered or banded gneiss
   b. Augen gneiss (containing eye-shaped structures around large crystals)
II. Migmatitic rocks
   a. Elements of a migmatite
      1. Leucosome (leucocratic part, usually granitic)
      2. Melanosome (melanocratic part, rich in mafic minerals)
   b. Structural types of migmatite
      1. Agmatitic (breccia-like migmatite)
      2. Dyktionitic (melanosome is extensively veined by leucosome)
      3. Stromatic (layered migmatite)
      4. Schollen (blocks or rafts of melanosome in leucosome)

minerals are used to describe the rock further. In addition to the textural and mineralogical information, chemical analyses of selected samples are done by XRF for comparison with other occurrences.

The terms melanocratic and leucocratic indicate the color index of the rock, hence the relative proportions of dark- to light-colored minerals (MacKenzie et al., 1982). Mafic and felsic may be applied to rocks which are composed predominantly of mafic minerals (olivine, pyroxenes, amphiboles, biotite, and opaque minerals) or of felsic minerals (potassium feldspar, plagioclase, and quartz), respectively.

The chemical classification and nomenclature of igneous rocks have been done by using total alkalis vs. silica (TAS) diagrams of Cox et al. (1979) for plutonic rocks (Fig. 13), and Le Maitre (1976, 1989) for volcanic rocks (Fig. 14). The terms ultrabasic, basic, intermediate, and acid are chemical terms to designate rocks with less than 45%, 45%–52%, 52%–66%, and more than 66% by weight of SiO_2, respectively (terms proposed by Peccerillo and Taylor, 1976).

STRUCTURAL GEOLOGY

Introduction

The purpose of structural core descriptions is to systematically identify, describe, and measure structural features, including bedding present in the core. Apart from the whole-round samples taken immediately after core recovery, material from both working and archive halves is examined. The responsibilities of shipboard structural geologists include:

1. documentation of all core structures and information concerning the relative timing of the various structural and diagenetic events;
2. recording the orientation of all structures on the core face and, wherever possible, orienting them in three dimensions in the core reference frame;
3. reorienting structural features from the core reference frame into a geographic framework by applying Tensor tool data,

Table 6. Textural terms for igneous rocks.

I. Attending to their crystallinity (degree of crystallization)

    1. Holocrystalline (100% crystals)
    2. Hypocrystalline or hypohyaline
    3. Hyaline (100% glass)

II. Attending to their granularity (grain size)

    1a. Phaneritic (all crystals of the principal minerals can be distinguished by the naked eye)
    1b. Aphanitic (all crystals, other than any phenocrysts present, cannot be distinguished by the naked eye)

    2a. Coarse grained (crystal diameters >5 mm)
    2b. Medium grained (crystal diameters 1-5 mm)
    2c. Fine grained (crystal diameters <1 mm)

    3a. Equigranular (all crystals are of approximately the same size)
    3b. Inequigranular (crystals differ substantially in size)

III. Attending to crystal shapes

    1. Euhedral (crystal completely bounded by its characteristic faces)
    2. Subeuhedral (crystal bounded by only some of its characteristic faces)
    3. Anhedral (crystal lacks any of its characteristic faces)

IV. Attending to mutual relations of crystals

    1. Seriate texture (crystals of the principal minerals show a continuous range of sizes)

    2. Porphyritic (relative large crystals [phenocrysts] surrounded by finer grained crystals of the groundmass)

    3. Poikilitic (relatively large crystals of one mineral enclose numerous smaller crystals of one or more other minerals). The host crystal is known as an oikocrystal (or enclosing crystal), and the enclosed crystals as chadacrysts

    4. Intergrowth textures (the junction between two crystals appears as a complex curve, and crystals are interdigitated or interlocked)

        a. Graphic texture (a regular intergrowth of two minerals producing the appearance of cuneiform writing)
        b. Symplectic texture (an intimate intergrowth of two minerals in which one mineral has a vermicular habit)
        c. Myrmekitic texture (patches of plagioclase intergrown with vermicular quartz often at the margin of a plagioclase crystal)

    5. Overgrowth textures (a single crystal has been overgrown either by material of the same composition, or by material of the same mineral species but different composition, or by an unrelated mineral)

        a. Corona texture (a crystal of one mineral is surrounded by a rim, or "mantle," of one or more crystals of another mineral)
        b. Crystal zoning (one or more concentric bands in a single crystal picked out by gradual or abrupt changes in composition of the crystal)

    6. Cavity textures (textures with holes in the rock or likely former holes now partly or completely filled with crystals)

        a. Vesicular texture (round elongated single and compound vesicles)
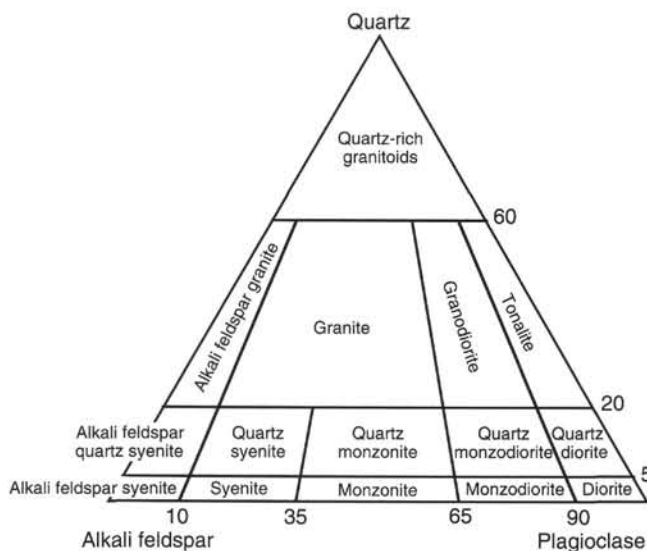   b. Amygdaloidal texture (former holes are occupied by late-stage magmatic and/or post-magmatic minerals)

Figure 12. Classification of plutonic rocks with a primary mineralogy consisting of plagioclase, alkali feldspar, and quartz.
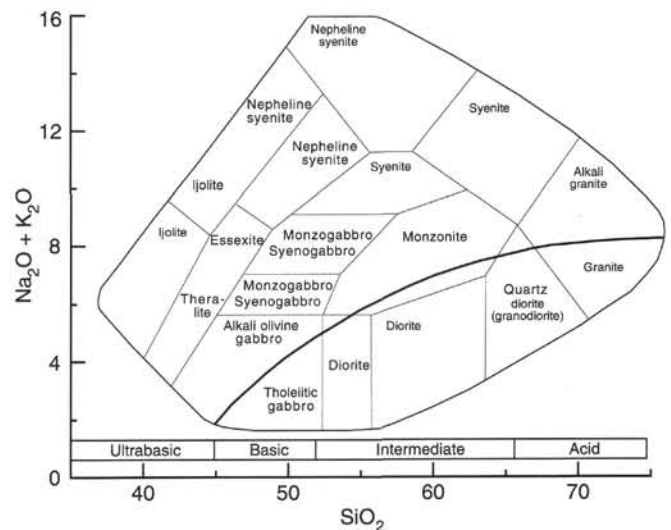

Figure 13. The chemical classification and nomenclature of plutonic rocks using total alkalis vs. silica (TAS) diagram of Cox et al. (1979). The curved bold line subdivides the alkalic from the subalkalic rocks. The TAS diagram divides rocks into ultrabasic, basic, intermediate, and acid on the basis of their silica content, following the usage of Peccerillo and Taylor (1976).

Formation MicroScanner (FMS) data, and primary remanent magnetization orientations, when available;

4. obtaining evidence from the style, geometry, and microstructure of individual structures that may have a bearing on the processes and conditions of deformation and on finite strain;

5. relating mineral assemblages to the microstructures in metamorphic rocks and to the recognized deformation events, in order to constrain the relationships between deformation and metamorphism;

6. constructing plausible interpretations of tectonic environments and deformation history within the limitations of the shipboard data set.
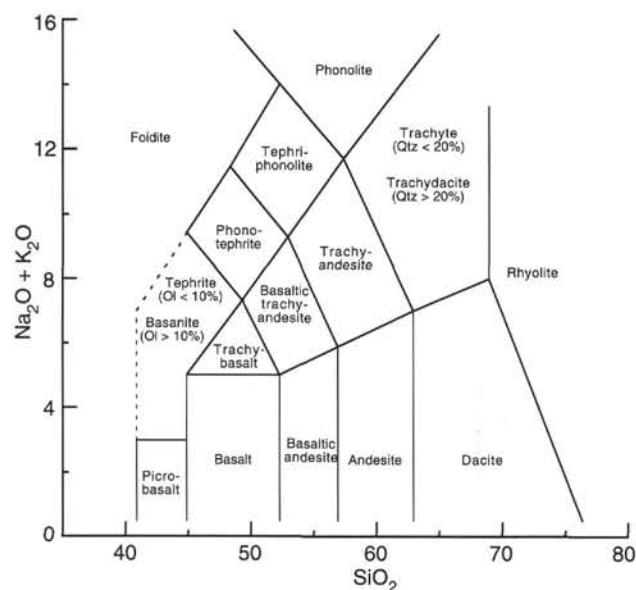
Figure 14. The chemical classification and nomenclature of volcanic rocks using the total alkalis vs. silica (TAS) diagram from Le Maitre (1989). Qtz = quartz, Ol = olivine.
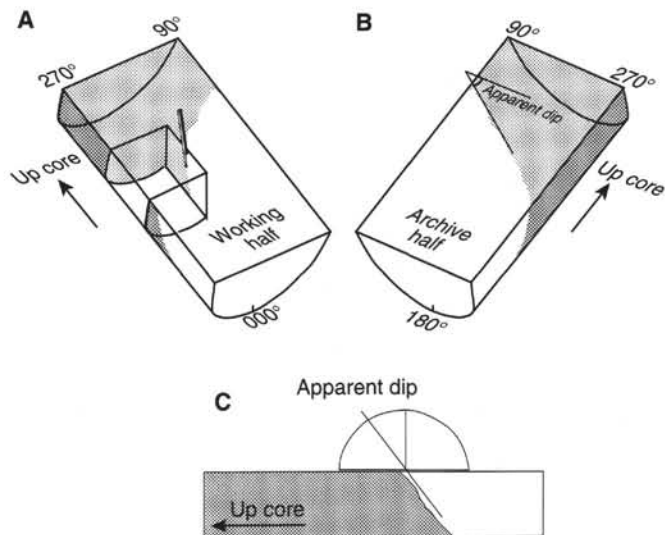

Figure 15. Diagram showing the conventions used in measuring azimuths and dips of structural features in cores and the techniques adopted for measuring structural planes in three dimensions in the core reference frame. The core reference frame conventions for the working half and the archive half of the core are seen in Figure 15A and 15B. The east-west apparent dip of the feature (in the core reference frame) was measured first, generally on the face of the archive half (Fig. 15B). The data were recorded as an apparent dip toward either 90° or 270° (270° in the example shown). A second apparent dip is measured on the outside of the core in a direction perpendicular to the core face, or on a fracture or cut made in the working half of the core (Fig. 15A). Note that cuts are normally considerably smaller than that shown in the diagram. The feature is identified on the new surface and the apparent dip in the north-south direction (core reference frame) marked with a toothpick. The apparent dip is quoted as a value toward either 000° or 180° (000° in the example shown). True dip and strike of the surface in the core reference frame are calculated from the two apparent measurements.

Limitations

Several problems are inherent in this type of study: incomplete core recovery, drilling-induced deformation, and rotation. Incomplete core recovery may lead to a sampling bias that is particularly acute for structural studies. For example, material from fault zones often is not recovered. When faulted rock is recovered, original deformation patterns may be disturbed. It can be difficult to distinguish between drilling-induced disturbance and tectonic features. Planar structures that traverse a core and are associated with preserved fault-rock may be regarded as original tectonic features rather than drilling-induced artifacts. In soft sediments, the degree of disruption of the bedding and other sedimentary structures, and the orientation of the structures relative to the side of the core liner can be used as an indication of core disturbance.

Features are initially oriented relative to local reference coordinates (i.e., the core liner reference frame; Fig. 15) and subsequently corrected to geographic north and vertical with the Tensor tool (APC cores only), paleomagnetic data, and Formation MicroScanner (FMS).

Formation MicroScanner (FMS)

The Formation MicroScanner (FMS) downhole logging tool is described in the "Downhole Logging" section, this chapter. FMS logging can be used most successfully for orientation purposes when, for example, regularly inclined bedding, or a single, regular joint pattern, can be recognized on downhole images and correlated with the core-derived data (e.g., MacLeod et al., 1992, 1994). These images are oriented with respect to geographical coordinates using built-in triaxial magnetometers. Comparing the features in the cores and on the logs thus allows the former to be reoriented from the core reference frame to geographical coordinates. Low recovery and the absence of distinctive markers in the borehole may inhibit correlation and reorientation. Detailed comparison of FMS data with the core data is usually done post-cruise.

Paleomagnetic Data

The direction of stable remanent magnetization can be used to reorient both individual sections of core on a small scale and in whole cores. It is especially useful for cores obtained by XCB or RCB coring, which typically recover contiguous pieces of core ranging from only a few centimeters up to ~1 m in length.

Tensor Tool Orientation

The Tensor tool provides frequent measurements of the direction and degree of deviation of the hole from the vertical. This tool allows orientation of APC cores only with respect to magnetic north. Measurements were obtained for only one of the 3–4 holes at each sapropel site.

Core Descriptions

Where structures are developed, the shipboard structural geologist makes a sketch of the core on the Structural Core Description Form. All observations and measurements are recorded in summary

form on the data table, using the codes defined in the accompanying Structural Terms Table (Table 7). Detailed structural geology observations can be found on the CD-ROM found in the back pocket of this volume. Core and section numbers are identified on both forms, allowing cross-referencing between the drawings, the data table, the core photographs, and other data.

Faults are distinguished on the basis of reasonable evidence for displacement, including truncation or offset of passive markers, the presence of fault gouge or breccia, and linear features on slip surfaces. Veins are characterized by their fill, width, presence or absence of an alteration halo, and their relationship to other deformational structures and fabrics. The orientations of structural features are noted relative to the core coordinates (Fig. 15).

Particular attention is paid to the character of fault breccias and fault gouges. The shape, size distribution, and lithological character of the fragments is described, as well as the character and structure of the matrix.

In metamorphic rocks, the way the core has been split may result in an artificial grouping of structural data when plotted in core coordinates (see "Metamorphic and Igneous Petrology" section, this chapter). This does not affect the possibility of reorienting the structures using FMS data.

Measurement of Structures

The orientation of structures is measured using a protractor-like graduated scale, with a pivoting, transparent measuring arm. During measurement, one half of the arm is aligned with the structure and the other half points to the value of the dip angle on the graduated scale. The apparent dip of features is measured on the split core-face, and if possible on another surface, either the outside of the core, or on a fracture or cut made preferably at right-angles to the split core-face (Fig. 15). The measurement of two different apparent dips on a structure allows the "true" dip and dip direction (in core coordinates) to be calculated, using, for example, the "Stereoplot" program.

The plane normal to the axis of the borehole is referred to as the apparent horizontal plane. On this plane a 360° net is used with a "pseudo-north" (000°) at the bottom line of the working half of the core. The face of the split core, therefore, lies in a vertical plane striking 090° (Fig. 15).

Structures in Metamorphic and Igneous Rocks

In metamorphic and igneous rocks the description of structural features visible in the core is carried out in conjunction with the petrological core description (see "Metamorphic and Igneous Petrology" section, this chapter). Small-scale structures (e.g., folds and microfolds, faults, shear zones, shear bands, asymmetric and symmetric boudinage, and porphyroclast systems) are drawn and noted and their significance noted in terms of the history and kinematics of the deformation. The orientations of the main foliation, mineral or stretching lineations on the foliation, and the axes, axial planes and sense of asymmetry of folds are systematically measured. Where visible, the relationships are noted between metamorphic minerals and the fabrics.

ORGANIC GEOCHEMISTRY

Concentrations of volatile hydrocarbons, inorganic (carbonate) carbon, and organic carbon, distributions of extractable long-chain alkenones, and the type of organic matter were determined during Leg 161. These analyses were made as part of the routine shipboard safety requirements and to provide preliminary information for shore-based organic geochemical research.

Table 7. List of structural features identified in cores and their abbreviations for use on the structural data form.

Structural feature	Identifier abbreviation	Planar or linear orientation measured
Drilling induced	DI	
Sedimentary bedding	SB	Bedding planes
Joints	J	Joint surface
Mineral veins	V	Vein margin
Magmatic vein	MV	Vein margin
Clastic veins	CV	Vein margin
Dikes	D	Dike margin
Fault, type unknown	F	Fault plane
Fault, normal	FN	Fault plane
Fault, reverse	FR	Fault plane
Fault, strike-slip	FSS	Fault plane
Fault striations	LF	Striation plunge and plunge direction
Breccia zone	BZ	Zone margin
Slaty cleavage	SC	Cleavage plane
Disjunctive cleavage	SD	Cleavage plane
Schistosity	SS	Schistosity
Mylonitic foliation	SM	Foliation plane
Gneissic foliation	SG	Foliation plane
Crenulation cleavage	SCC	Cleavage plane
Cataclastic foliation	SCF	Foliation plane
Magmatic planar fabric	SI	Foliation plane
Stylolites	ST	Stylolite planes
Mineral lineation	LM	Lineation plunge and plunge direction
Stretching lineation	LS	Lineation plunge and plunge direction
Crenulation lineation	LC	Lineation plunge and plunge direction
Intersection lineation	LI	Lineation plunge and plunge direction
Fold	Fo	Fold axial plane and hinge line
Slump fold	SFo	Fold axial plane and hinge line
Boudinage	Bo	Axis of boudins
Ductile shear zone	SZ	Shear zone margin

Volatile Hydrocarbons

Low-molecular-weight hydrocarbon samples were obtained by two different methods. The routine headspace procedure (Kvenvolden and McDonald, 1986) involved about 5 cm^3 of sediment being taken from each core and put into a 21.5-cm^3 glass serum vial. The vial was sealed with a septum and a metal crimp cap and heated at 60°C for 30 minutes. A 5-cm^3 volume of gas from the headspace in the vial was extracted with a glass syringe for analysis by gas chromatography.

A vacutainer method of gas collection (Kvenvolden and McDonald, 1986) was used where gas pockets or expansion voids were visible in the core while it was still in the core liner. A gas syringe needle was used to penetrate the core liner, and an attached vacutainer collected the gas.

Headspace and vacutainer gas samples were both typically analyzed using a Hewlett Packard 5890 II Plus gas chromatograph (GC) equipped with a 2.4-m × 3.2-mm stainless steel column, packed with HaySep S (80–100 mesh), and a flame ionization detector (FID). This instrument quickly measures the concentrations of methane, ethane, ethene, propane, and propene. Either the vacutainer or the headspace syringe was directly connected to the GC via a 1.0-cm^3 sample loop. Helium was used as the carrier gas, and the GC oven was held at 90°C. Data were collected and evaluated with a Hewlett-Packard 3365 Chemstation data-handling program. Calibrations were done using Scotty IV analyzed gases, and gas concentrations were measured in ppm.

When higher concentrations of C_{2+} hydrocarbons were suspected, gas samples were analyzed with the Natural Gas Analyzer (NGA), which measures hydrocarbons from methane to hexane. This system consists of a Hewlett-Packard 5890 II Plus gas chromatograph equipped with a 60-m × 0.32-mm DB-1 capillary column and an FID. Non-hydrocarbon gases could be analyzed at the same time via a packed column and a thermal conductivity detector (TCD). For hy-

drocarbon analysis, the GC oven was heated from 80°C to 100°C at 8°C/min and then to 200°C at 30°C/min. Helium was the carrier gas, and a Hewlett Packard Chemstation data system was used.

Elemental Analysis

Three 5-cm³ sediment samples were routinely selected from each core for analysis of total carbon (TC), carbonate carbon, total organic carbon (TOC), nitrogen, and sulfur. Additional samples were taken from intervals of special interest, particularly dark-colored and presumably organic matter-rich sediments (sapropels), and were similarly analyzed.

Carbonate carbon concentrations of the samples were determined using a Coulometrics 5011 carbonate carbon analyzer. A sample of about 15 mg of freeze-dried, ground material was reacted with 2N HCl in this system. The liberated CO_2 forms a titratable acid with a blue monoethanolamine indicator solution that causes the color to fade. The change in color is measured by a photodetector cell that automatically stimulates a platinum anode to return the solution to a basic pH, which in turn returns the indicator to its original color. Carbonate contents are expressed as weight percent $CaCO_3$, assuming that all the carbonate was present as calcite.

Total carbon, nitrogen, and sulfur were determined using a Carlo Erba 1500 CNS Analyzer. About 5 mg of freeze-dried, ground sediment was combusted at 1000°C in a stream of oxygen. Nitrogen oxides were reduced to N_2, and the mixture of SO_2, CO_2, and N_2 was separated by gas chromatography and quantified with a thermal conductivity detector. TOC concentrations were determined as the difference between carbonate carbon and the TC concentrations. Atomic organic matter C/N ratios were calculated from the TOC concentrations and the total nitrogen concentrations.

Extractable Long-Chain Alkenones

Sea-surface paleotemperatures were estimated by measuring the relative abundances of the long-chain di- and tri-unsaturated alkenones, using a calibration curve based on analyses of suspended particulate matter from the Mediterranean Sea (Ternois et al., unpubl. data). Extractions of 1–2 g of freeze-dried organic matter-rich sediment were done using 3 ultrasonic extractions with dichloromethane/methanol (99/1) for 10 min. The sediment-solvent mixture was centrifuged, and the solvent removed by pipet to a vial. The three extracts were combined, and then they were evaporated under a stream of nitrogen on a hot plate at 40°C. The isolated extract was redissolved in 50–100 μL of hexane and then analyzed by gas chromatography on a Hewlett-Packard Model 5890 II Plus gas chromatograph equipped with a 50-m × 0.2-mm HP Ultra 1 (Cross-Linked Methyl Silicon Gum) capillary column (0.11 μm film thickness). Operating conditions were: Injector temperature, 250°C; detector temperature, 300°C; temperature program, 30°C (3 min), 10°C/min to 220°C, 4°C/min to 300°C (15 min). Usually, 2–3 μL were injected in the splitless mode. Identifications of alkenones were based on comparison with chromatograms in published literature (e.g., Brassell et al., 1986; Prahl and Wakeham, 1987; Prell, Niitsuma, et al., 1989).

Organic Matter Type

The type of organic matter was evaluated by pyrolysis using the Delsi-Nermag Rock-Eval II system. This procedure uses a whole-rock pyrolysis technique to identify the type and maturity of organic matter and detect the petroleum potential of the sediments (Espitalié et al., 1986). The Rock-Eval system involves a temperature program that first releases volatile hydrocarbons (S_1) at 300°C for 3 min and then releases hydrocarbons from thermal cracking of kerogen (S_2) as

the temperature increases from 300°C to 600°C at 25°C/min. S_1 and S_2 hydrocarbons are measured by an FID and reported in milligrams per gram of sediment. The temperature at which the kerogen yields the maximum amount of hydrocarbons during the S_2 program provides T_{max}, a parameter which assesses the maturity of the organic matter. Between 300°C and 390°C of the pyrolysis program, CO_2 released from the thermal degradation of organic matter (S_3) is trapped and measured by a TCD in milligrams per gram of sediment. Rock-Eval II parameters characterize organic matter by allowing the following indices to be calculated: Hydrogen Index (HI), $(100 \times S_2)$/TOC; Oxygen Index (OI), $(100 \times S_3)$/TOC; S_2/S_3 ratio; Production Index (PI), $S_1/(S_1 + S_2)$; and Petroleum Potential (PC; pyrolyzable carbon), $0.083 (S_1 + S_2)$. Interpretation of Rock-Eval data is considered to be unreliable for samples containing less than 0.5% TOC (Peters, 1986). A Hewlett-Packard 3365 Chemstation computer data analysis system was used to integrate and store the results obtained from the Rock-Eval analyses.

Further characterization of the organic matter type was performed by pyrolysis-gas chromatography using a Geofina Hydrocarbon Meter (GHM). This instrument employs a Varian 3400 gas chromatograph that has been modified to include a programmable pyrolysis injector. The system has FIDs and two capillary columns (25 m, GC2 fused silica). Like the Rock-Eval II, this instrument determines S_1, the free hydrocarbons (and similarly volatile compounds) that are released up to 300°C, and S_2, the pyrolysis products that are generated from the sample kerogen. In addition, the effluent of the furnace is split 20:1 so that the hydrocarbon distributions making up S_1 and S_2 can be examined in detail by capillary gas chromatography.

INORGANIC GEOCHEMISTRY

Shipboard interstitial water analyses were performed on 5- to 15-cm-long whole-round sections that were cut on deck immediately after core retrieval. Samples were taken from the bottom of section three of every core for the first one hundred meters of one of the holes and from every third core thereafter. Interstitial waters were collected using a titanium squeezer (modified after Manheim and Sayles, 1974). Before squeezing, each whole-round surface was carefully scraped with a spatula to remove potential contamination. After loading the squeezer, pore waters were extruded by applying pressures up to 40,000 pounds (approximately 4150 psi) using a hydraulic press. Interstitial water samples were collected into 50 mL plastic syringes and subsequently filtered through 0.45 μm Gelman polysulfone disposable filters and stored in plastic vials prior to analysis. Aliquots for shore-based analyses were placed in heat-sealed acid-washed plastic tubes and glass ampules.

Interstitial water samples were routinely analyzed for salinity, as total dissolved solids (‰), with a Goldberg optical hand-held refractometer (Reichart); pH and alkalinity by Gran titration with a Brinkmann pH electrode and a Metrohm autotitrator; chloride by titration with visual and potentiometric end-point determination; calcium and magnesium concentrations by titration; and silica, phosphate, and ammonium by spectrophotometric methods with a Milton Roy Spectronic 301 spectrophotometer (Gieskes et al., 1991). International Association of Physical Sciences Organizations (IAPSO) standard seawater was used for calibrating most techniques, and for determining 1-σ standard deviations. These standard deviations were: alkalinity, <1.5%; chloride, 0.4%; calcium, <1%; magnesium, 0.5%; and silica and ammonia, 4% to 5%. At all sites, sodium was determined using charge balance calculations where Σ (cation charge) = Σ (anion charge).

Additionally, potassium, magnesium, calcium, sulfate, and bromide were analyzed by ion chromatography using a Dionex DX-100.

The 1-σ standard deviations were: potassium, <3%; magnesium and calcium, <3%, and sulfate and bromide, <4%.

Lithium, potassium, sodium, and strontium concentrations were quantified using flame atomic emission (AES) and absorption spectrometry (Varian SpectrAA-20). Lithium and strontium were determined on 1/10 diluted samples, potassium, and sodium on 1/200 diluted samples using an air-acetylene (Li, K, Na) and nitrous oxide acetylene flame (Sr). Standards for all flame AES techniques were matched in matrix composition to the samples. The 1-σ standard deviations were: lithium, 1%–2%; and potassium, sodium, and strontium, <2%–3%. A more detailed description of all methods and standards used is given in Gieskes et al. (1991).

PHYSICAL PROPERTIES

The principal objectives for the physical properties measurements are: (1) to provide high-resolution physical data of the sediments, (2) to determine the effects of sedimentological and textural changes on the physical properties, (3) to calibrate downhole logs, (4) to constrain the interpretation of seismic reflection data, and (5) to provide hole-to-hole depth correlation for multiple-hole APC-cored sites. Tables containing all physical properties data are on the CD-ROM found in the back pocket of this volume.

Non-destructive high-resolution measurements of whole-round core sections were obtained from the multisensor track (MST). Thermal conductivity was measured using the needle-probe technique on the whole-round core sections.

In unlithified sediments, *P*-wave velocity was measured on the working half of the core. In the more lithified sediments and hard-rock samples, thermal conductivity was measured using a half-space needle probe method, and *P*-wave velocities were determined from cut pieces of the sediment and hard-rock samples. Throughout the core, index properties (water content, wet- and dry-bulk density, grain density, porosity, and void ratio) were determined from discrete samples. After measurement, some of the dried samples were also used for geochemical analyses (see "Inorganic Geochemistry" section, this chapter).

Multisensor Track (MST)

The MST incorporates the Magnetic Susceptibility Meter (MSM), gamma-ray attenuation porosity evaluator (GRAPE), *P*-Wave Logger (PWL), and Natural Gamma Ray device (NGR). The sampling rate was typically one measurement every 0.5 to 2.5 cm for GRAPE, 3 cm for magnetic susceptibility, 10 cm for natural gamma-ray radiation, and 3 cm for the *P*-wave velocity. MST data are located on the CD-ROM found in the back pocket of this volume.

Magnetic susceptibility was measured using the 0.1 range on the Bartington Model M.S.1 susceptometer with an 8-cm-diameter loopsensor (M.S.1/CX80). The small sampling interval for magnetic susceptibility was chosen for maximum utility in hole-to-hole correlation.

The GRAPE took measurements of bulk density at discrete intervals by comparing attenuation of gamma rays through the cores with attenuation through an aluminum standard (Boyce, 1976). Generally, the GRAPE data were most reliable in APC and non-biscuited XCB and RCB cores.

The PWL transmits 500-kHz compressional-wave pulses through the core. The transmitting and receiving transducers were aligned perpendicular to the core axis. A pair of displacement transducers monitors the separation between the compressional wave transducers. Variations in the outside diameter of the liner do not degrade the accuracy of the velocities; but the PWL does not provide accurate measurements on cores that do not completely fill the core liner.

Natural gamma radiation measurements are used for correlation between the cores and the downhole well logs. Due to time constraints, NGR measurements were made only at one hole per site, for 15 s at each 10-cm-spaced sampling point.

Thermal Conductivity

The thermal conductivity was measured using the needle-probe method, in full-space configuration in whole-core sections for soft sediments (von Herzen and Maxwell, 1959), and in half-space configuration on split cores (Sass et al., 1984; Vacquier, 1985), for lithified sediments and hard rock samples. All measurements were made after the cores had equilibrated to the laboratory temperature. Data are reported in units of W/(m·K), and have an estimated error of 1%–3% for the standard needle-probe technique and 5%–10% for the half-space technique.

Needle probes containing a heating wire and a calibrated thermistor were inserted into the sediment through small holes drilled in the core liners before the sections were split. This allowed up to four probes to be connected and operated simultaneously. For each run, we used probes in the sediment and one in a conductivity standard.

At the beginning of each test, temperatures in the samples were monitored until the background thermal drift was determined to be less than 0.04°C/min. The heater element was turned on and the temperature rise in the probes was recorded. Thermal conductivities were calculated from the subsequent rate of temperature rise.

After the heater had been on for about 20 s, the needle-probe response was very close to that of a line source with constant heat generation per unit length. Temperatures recorded during a time interval of 60–300 s were fit using a least-squares technique to the appropriate equation:

$$T(t) = (q/4\pi k) \times \ln(t) + L(t)$$

where k is the apparent thermal conductivity, T is temperature, t is time, and q is the heat input per unit length of wire per unit time. The term L(t) describes a linear change in temperature with time, and includes the background temperature drift. The lower time limit was chosen to avoid starting transient terms related to the finite length of the heater, which only approximates an infinite line source, and the upper time limit from the edge effects of the cores, which are not full-space mediums.

Half-space measurements were made on selected lithified sediments and crystalline rock samples after the cores were split and the face of the split core was polished. The needle probe rested between the polished surface and a grooved epoxy block with relatively low conductivity (Sass et al., 1984; Vacquier, 1985). Half-space measurements were conducted in a water bath to keep the samples saturated, improve the thermal contact between the needle and the sample, and to reduce thermal drift. Additionally, EG&G thermal joint compound was used to improve the thermal contact. The data collection and reduction procedures for half-space tests were similar to those for full-space tests, except for a multiplicative constant in the above equation that accounts for the different experimental geometry.

P-wave Velocity

In addition to the MST measurements, compressional (*P*-wave) velocities were determined on discrete samples. Depending on the degree of sediment lithification, two different measurements were

used. Travel times were measured in softer sediment using a Dalhousie University/Bedford Institute of Oceanography Digital Sound Velocimeter (Mayer et al., 1988; Courtney and Mayer, 1993). The velocity calculation was based on the measurement of the travel time of an impulsive acoustic signal traveling between two pairs of piezoelectric transducers inserted in the split sediment cores. One transducer pair, mounted with a fixed separation (approximately 7.0 cm), was positioned parallel to the core axis. The other transducer pair, also with a fixed separation (approximately 3.5 cm), was positioned perpendicular to the core axis. The source signal used was a 0.1μs square wave with a period of 0.2 ms. The received signals were stacked 10–20 times to improve the signal-to-noise ratio. Temperature of the unlithified sediments was measured with a digital thermometer probe. Corrections for electronic delay time were made using standard aluminum samples of various lengths and water at known temperatures.

When the material became too consolidated to insert the Digital Sound Velocimeter (DSV) transducers, measurements perpendicular to the axis of the core were made through the core liner with the Hamilton Frame velocity transducer. Typically, there was a depth interval where the sediment was too consolidated to insert the DSV transducers without cracking the sediment, but was not sufficiently stiff to utilize the Hamilton Frame. Velocity data were reported here in raw form, but corrections for in situ temperature and pressure could also be made using the relationships in Wyllie et al. (1956).

Index Properties

Index properties (water content, wet- and dry-bulk density, grain density, porosity, and void ratio) were typically determined from one sample (about 10–15 cm³) from each section of the first deep hole at each site. These samples were taken at or near the locations of the compressional wave velocity measurements. Subsequent holes at each site were sampled at a rate of 1–2 samples per core.

The samples were placed in aluminum containers pre-calibrated for weight and volume. Sample weights were determined to a precision of ±0.005 g using a Scitech electronic balance. Volumes were determined using a helium-displacement Quantachrome Penta-Pycnometer. Dry weight and volume measurements were performed after the samples were oven-dried at 110°C for 48 hr and allowed to cool in a desiccator.

Index properties were calculated from measurements of the wet and dry masses of the sample and from the volume. At the first site, index properties were calculated using two different methods described in the ASTM designation (D) 2216 (American Society of Testing and Materials, 1989; Hamilton, 1971; Boyce, 1976). Method "B" uses weights of the wet and dry sample and volume of the wet sample. Method "C" uses the volume of the dry sample and the sample wet and dry weights. Method "B" gave higher than expected grain densities and a large scatter in the other calculated index properties. For this reason, only method "C" was used for subsequent sites.

DOWNHOLE LOGGING

The Lamont-Doherty Earth Observatory Borehole Research Group (LDEO-BRG) in conjunction with Schlumberger Well Logging Services provided the geophysical well logging aboard the *JOIDES Resolution*. Primarily designed for use in hydrocarbon exploration, logging tools have been adapted to meet ODP requirements and hole conditions. This includes the reduction of tool diameter to allow insertion into the 3.8-in drill-string bore. On Leg 161, we used the quad combo, the Formation MicroScanner (FMS),

the Geological High-Sensitivity Magnetic Tool (GHMT), and Geochemical Logging Tool (GLT).

Downhole logs are used to determine directly the physical, chemical, and structural properties of formations penetrated by drilling. Log data are collected continuously, and interpretation of these continuous in situ measurements allow for quantification of the formation's stratigraphic, lithologic, geophysical, and mineralogic characteristics. When core recovery is incomplete, log data may serve as a proxy for physical properties and sedimentological data and permit the core to be placed in its proper stratigraphic position within the cored interval. Logs also complement discrete core measurements and offer the additional advantage over core-based analyses in that they are rapidly collected and represent continuous in situ measurements. Geophysical well-logging is also used to aid in characterization of sedimentary sequences when integrated with core and seismic reflection data.

Well-Logging Operations

After coring was completed, the holes were flushed of sediment fill by circulating a pill of heavy viscous drilling fluid through the drillpipe to the mudline. The drilling assembly was pulled up to the upper logging point (~80–100 mbsf), and then it was run down to the bottom of the hole again to condition the borehole for logging. Tool strings comprising one or more combinations of sensors were then lowered downhole using a 7-conductor cable. When necessary, a wireline heave-motion compensator (WHC) was employed to minimize the effect of ship's heave on the tool position in the borehole.

Logging Tool Strings

When a tool string (a combination of several sensors) was lowered down the hole on a conductor cable, each of the sensors continuously monitored some property of the formation or borehole. The data were typically recorded at 0.1524-m vertical intervals. The depths of investigation into the formation (and the vertical resolution) were sensor-dependent (Table 8).

For Leg 161, incoming data from the geophysical and the FMS tool strings were acquired, archived, and monitored in real time on the Maxis 500 logging computer. The GLT was collected with the "old" OSU unit (offshore service unit). Data from the MAXIS 500 are generated in a Digital Log Information Standard format (DLIS). This was converted to LIS format (Log Information Standard) for compatibility with onboard and shore-based logging software. After logging, data were transferred to a Sun workstation and Macintosh computers for preliminary shipboard correlation and interpretation.

Individual logging tools were combined in five different strings (Fig. 16) during Leg 161: the Seismic-Stratigraphic tool (NGT, LSS/SDT, DITE, TLT), the Lithoporosity tool (NGT, CNT-G, HLDT/CALI, TLT), the GLT, the FMS, and the GHMT. In addition, the Borehole Televiewer (BHTV) was also used in basement and deeper penetration holes in the Alboran Sea. The Lamont-Doherty Earth Observatory (LDEO) temperature tool was attached, whenever possible, to the base of tool strings to obtain borehole temperatures. The Natural Gamma-Ray Tool (NGT) was run as part of each tool string to correlate depths between different logging runs.

The seismic stratigraphic and lithoporosity strings can be combined into a single string termed the quad combo. It reached a total length of 31 m (33 m with the TLT), making it difficult or impractical to run in short holes. In some cases, using the seismic stratigraphic tool and the lithoporosity tool separately also improves the quality of the sonic and neutron porosity logs. The sonic tool in the seismic stratigraphic tool string requires a centralizer for optimum perfor-

Table 8. Approximate vertical resolution of various logging tools used during Leg 161.

Tool	Vertical resolution	Depth of investigation
Phasor induction tool (DIT)		
ILD Deep resistivity	200 cm, 88 cm, 59 cm	1.5 m
ILM Medium resistivity		
SFL Shallow focused		
	150 cm, 88 cm, 59 cm	76 cm
	59 cm	38 cm
Natural gamma-ray tool (NGT)	46 cm	Variable
	15–30 cm	
Lithodensity tool (HLDT)		Variable
Density, photoelectric effect		15–60 cm
	49 cm (6-in sample)	
	35 cm (2-in sample)	
	20 cm alpha processing	
	30 cm alpha processing (2 in)	
Dipole shear imager (DSI)	30 cm	Variable
	Special processing 15 cm	10–60 cm
Sonic digital tool (SDT-C/array)	30 cm	Variable
	Special processing 15 cm	10–60 cm
Gamma-ray spectroscopy tool	15 cm	Variable
(GST)		12–20 cm
Aluminum activation tool (AACT)	25 cm	Variable
		12–20 cm
Dual porosity compensated	55 cm (6-in sample)	Variable and porosity dependent
neutron tool (CNT-G)	33 cm alpha proc. (6-in sample)	
	25.4 cm alpha proc. (2-in sample)	(15–60 cm)
Formation MicroScanner (FMS)	5 mm	5–25 cm
Lamont temperature tool	(a) fast-response reading (1-s time constant)/s (b) slow-response, high-accuracy reading (10-s time constant)/10 s; vertical resolution depends on logging speed.	

Notes: Final processed GLT is in fact between 0.3 and 1 m. Standard sampling is at 15-cm (6-in) intervals. High resolution sampling is at 5.5-cm (2-in) intervals. Alpha processing is a special high-resolution processing routine. Depth of investigation is dependent upon the formation and borehole environment; these values are only estimates.

mance, while the neutron porosity tool in the lithoporosity tool string performs best when in direct contact with the borehole wall.

Logging Tools

A brief description of logging tools used during Leg 161 is given in the following sections. A detailed description of logging tool principles and applications was provided in Ellis (1987), Schlumberger (1989), and Timur and Toksöz (1985). The specifics of each tool are summarized in Table 8.

Natural Gamma-Ray Spectrometry Tool (NGT)

The NGT measures the natural radioactivity of the formation using a NaI scintillation crystal mounted inside the tool. In formations, gamma-rays are emitted by the radioactive isotope ^{40}K and by the radioactive elements of the U and Th decay series. Measurements are analyzed by dividing the incident gamma-ray signature into five discrete energy windows that correspond to the main spectral peaks for each element. The total counts recorded in each window, for a specified depth in the well, are inverted to give the elemental abundances of K (wt%), U (ppm), and Th (ppm). The NGT also provides a measure of the total gamma-ray signature (SGR or [K + U + Th]) and a uranium-free measurement (CGR or [Th + K]). The tool has a vertical resolution on the order of 0.46 m.

The natural gamma-ray measurement is commonly used to estimate the clay or shale content of a formation since there is a relatively
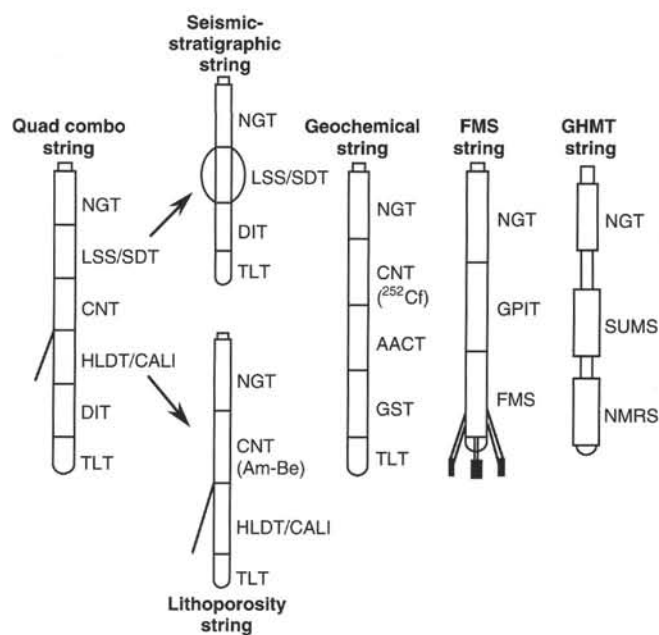

Figure 16. Schematic diagram of Schlumberger logging tool strings used on Leg 161. Tool strings are not drawn to scale.

high abundance of radioactive elements in clay minerals. There are rock matrices, however, for which the radioactivity ranges from moderate to extremely high values because of the presence of volcanic ash, potassic feldspar, or other radioactive minerals. In addition, U/Th ratios from NGT data are used as indicators of organic carbon content and allow changes in the oxidation state of diagenetic minerals to be determined.

Phasor Dual Induction–Spherically Focused Resistivity Tool (DITE-SFL)

The DITE-SFL provides three different measurements of electrical resistivity, each of which penetrates the formation to a different depth and has different vertical resolution (Table 8).

Water content and salinity are the most significant factors controlling the resistivity of rocks. Resistivity, therefore, is related primarily to the inverse square root of porosity (Archie, 1942). Other factors influencing the resistivity of a formation include the concentration of hydrous and metallic minerals, hydrocarbons and gas hydrates, and the abundance, distribution, and geometry (tortuosity) of interconnected pore spaces.

Long Spaced Sonic Tool (LSS/SDT)

The LSS measures the time required for acoustic waves to travel through the formation between an array of transmitters and receivers separated by vertical distances ranging from 0.91 m to 3.66 m. It provides a direct measurement of acoustic velocity through sediments from the interval transit time (ΔT), and it is likely to yield measurements free from the effects of formation damage caused by drilling. Sound velocity is related to sediment porosity and lithification and/or compaction. In conjunction with density logs or core physical property measurements, sonic logs can be used to compute synthetic seismograms.

High-Temperature Lithodensity Tool (HLDT)

The HLDT uses a ^{137}Ce gamma-ray source and measures the resulting gamma-ray flux at fixed distances from the source. Under normal operating conditions, attenuation of gamma rays is primarily caused by Compton scattering, which is related to electron density. Formation density is inferred from this gamma-ray flux by assuming a direct relationship between electron density and bulk density, and also that the ratio of atomic weight and the atomic number for most common rock-forming elements is constant (about 2.1).

The photoelectric absorption effect is used as an indicator of matrix lithology that is independent of porosity. Photoelectric absorption occurs at gamma-ray energies below which Compton scattering can usually occur (<100 keV). Besides being energy dependent, the probability of photoelectric absorption occurring depends on the atomic number of a formation (e.g., it is more sensitive to elements with higher atomic numbers). The magnitude of this measurement is therefore related to the abundance of the heavier "matrix" (mineral) portion of a formation, and for this reason it is almost entirely independent of porosity. The radioactive source and detector array is placed in a tool that is pressed against the borehole wall by a strong spring arm. If the hole is excessively rough, some drilling fluid will infiltrate between the detector and the formation. Consequently, density readings can be artificially low. Approximate corrections can be applied using caliper data. The vertical resolution is given in Table 8.

Compensated Neutron Porosity Tool (CNT-G)

Neutron logs are used principally to determine formation porosity. The CNT-G uses a 16 Curie Am-Be chemical source, which bombards the formation and borehole with fast neutrons (4.5 MeV). Two pairs of sensors detect the number of neutrons (count rates) in the epithermal (0.1–100 eV) and thermal (<0.025 eV) energy ranges. The emitted neutrons interact elastically with the surrounding atoms, and the greatest energy loss occurs with atoms of small capture cross-section, in particular hydrogen atoms (almost the same mass as one neutron). Thus the slowing-down and capture of the emitted neutrons is primarily controlled by the amount of hydrogen surrounding the tool. This hydrogen resides almost entirely in water molecules. The tool is designed to be run against the borehole wall. When used in the quad combo, where the tool is not fully against the borehole wall, CNT-G data should be interpreted with caution. Poor tool contact with the borehole wall also leads to an overestimated formation porosity because, in addition to the borehole water, neutrons are strongly absorbed by Cl.

Both mineral-bound water (e.g., clay minerals) and water filling the pore space affect tool response, commonly leading to an overestimate of true porosity. Free water content (porosity) is determined from the thermal neutron counts. Water that is structurally bound can be estimated by subtracting free water from the total water estimates. Neutron logs are also affected to some extent by matrix lithology of the formation. When the borehole fluid is gas charged, this effect is reduced to a negligible level. However, these effects and those caused by the amount and type of hydrocarbon can be recognized and corrected for only if additional porosity information from sonic and/or density logs is available.

Geochemical Logging Tool String (GLT)

The geochemical logging tool string (GLT) consists of four separate logging tools: the natural gamma-ray spectrometry tool (NGT), the compensated neutron tool (CNT), the aluminum activation clay tool (AACT), and the gamma-ray spectrometry tool (GST). A schematic drawing of the GLT, which was run in Holes 974C, 975C and 976B on Leg 161, is shown in Figure 17. (All tool names are trademarks of Schlumberger.) These four tools use three separate modes

TCCB — Telemetry cartridge

NGT — **Natural gamma-ray tool**: measures naturally radioactive elements Th, U, and K

Dual-porosity compensated neutron tool: measures neutron porosity in the thermal and epithermal energy ranges

— Thermal detectors

CNT-G — Californium 252 source

— Epithermal detectors

AACT — **Aluminum activation clay tool**: measures aluminum activation and natural count rates as it passes the formation activated by Californium 252

Gamma-ray spectrometry tool: measures concentration of Ca, Si, Fe, S, Gd, Ti, H, Cl, and formation capture cross-section

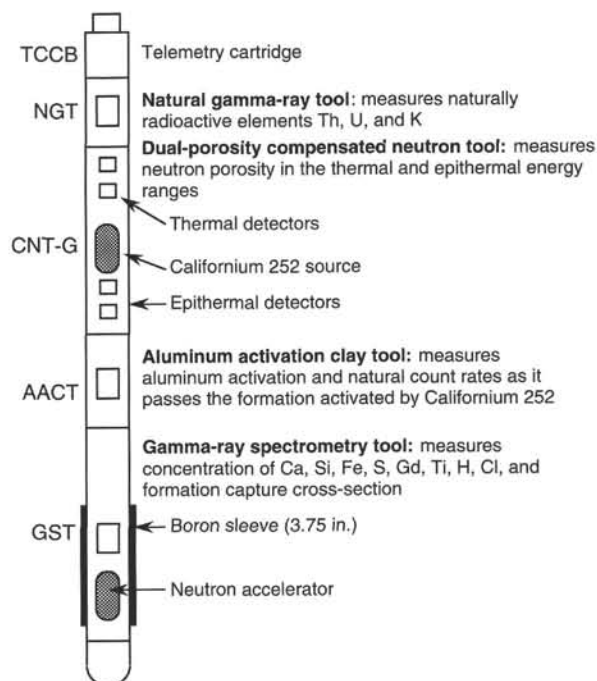GST — Boron sleeve (3.75 in.)

— Neutron accelerator

Figure 17. Schematic drawing of the Schlumberger geochemical logging tool string used in the Ocean Drilling Program.

of gamma-ray spectroscopy for a comprehensive elemental analysis of the formation. The NGT is located at the top of the tool string so that it can measure the naturally occurring radio nuclides, thorium (Th), uranium (U), and potassium (K), before the formation is irradiated by the nuclear sources contained in the lower tools. The CNT, located below the NGT, carries a californium (^{252}Cf) neutron source to activate the Al atoms in the formation. The AACT, a modified NGT, is located below the ^{252}Cf source, measuring the activated gamma rays in the formation. By combining the AACT measurement with the previous NGT measurement, the background radiation is subtracted out and a reading of formation Al is obtained (Scott and Smith, 1973). The gamma-ray spectrometry tool, at the base of the string, carries a pulsed neutron generator to induce prompt-capture gamma-ray reactions in the borehole and formation and an NaI(Tl) scintillation detector to measure the energy spectrum of gamma rays generated by the prompt neutron capture reactions. As each of the elements in the formation is characterized by a unique spectral signature, it is possible to derive the contribution (or yield) of each of the major elements silicon (Si), iron (Fe), calcium (Ca), titanium (Ti), sulfur (S), gadolinium (Gd), and potassium (K) from the measured spectrum and, in turn, to estimate the relative abundance of each in the formation when combined with the elemental concentrations from the NGT and AACT (Hertzog et al., 1987). The GST also measures the hydrogen (H) and chlorine (Cl) in the borehole and formation, although these elements are not directly used for determining the rock geochemistry.

The only major rock-forming elements not measured by the geochemical tool string are magnesium (Mg) and sodium (Na); the neutron-capture cross sections of these elements are too small relative to their typical abundance for the GLT to detect. A rough estimate of Mg + Na can be made in some instances by using the photoelectric factor (PEF), measured by the lithodensity tool (Hertzog et al., 1987). This calculation was not implemented on the Leg 161 geochemical data as the (Mg + Na) component was generally below the detection resolution of this technique (Pratson et al., 1993).

Formation MicroScanner Tool (FMS)

The FMS tool produces high-resolution micro-resistivity measurements from which images of the borehole are produced. These can be used for detailed sedimentological or structural interpretations. The tool consists of four orthogonal pads, each with sixteen 6.7-mm-diameter electrodes. Pad electrodes are spaced about 2.5 mm apart and are arranged in two diagonally offset rows of eight electrodes each. These four pads are pressed against the borehole wall. A focused electrical current flows between buttons and is recorded as a series of curves that reflect the micro-resistivity variations of the formation. The FMS tool string also contains a General-Purpose Inclinometry Tool (GPIT) that orients the resistivity measurements through the use of a three-component magnetometer and accelerometer that respond to the declination and inclination of the earth's magnetic field, so that the orientation of the interpreted sedimentary or structural features with respect to geographical coordinates can be determined easily.

Processing converts the measurements into spatially oriented images of the borehole wall, using information from the GPIT. Further processing can provide oriented measurements of strike and dip of planar features. The vertical resolution of the FMS is about 5 mm. The tool pads cover approximately 22% of the borehole wall for each pass. Use of the FMS is restricted to hole diameters of less than 37 cm.

FMS images may be used for detailed correlation of core and log depths, for core orientation, mapping of fractures, faults, foliations and formation structures, as well as determining strikes and dips of bedding. The FMS can also provide information on the orientation of the in situ stress field, by imaging the directions of borehole breakouts and by providing precise measurements of borehole diameter in two orthogonal directions.

Lamont-Doherty Temperature Logging Tool (TLT)

The TLT is a high-precision self-contained temperature recording tool that can be attached to any Schlumberger tool string. Data from two thermistors and a pressure transducer are collected at a predetermined rate of one sample per second and stored within the tool. A fast-response, lower accuracy thermistor is able to detect sudden temperature excursions caused by fluid flow from the formation. A slow-response, higher accuracy thermistor can be used to estimate borehole fluid temperature. Data are recorded as a function of time, with conversion to depth based on pressure recordings from the pressure transducer and on the synchronized time-depth record of the wireline cable. Once the in situ measurement is completed, data are transferred from the tool to a shipboard computer for analysis. Macintosh-based software was used for the processing of temperature data.

Geological High-Sensitivity Magnetic Tool String (GHMT-A)

This tool was developed jointly by Schlumberger, French government research institutions (CEA-LETI and CNRS-ENS), and TOTAL. The tools were designed and constructed by a branch of the French Atomic Energy Commission (CEA-LETI), which also developed the analysis software.

The GHMT-A comprises a high sensitivity total magnetic field sensor (NMRS) coupled with a magnetic susceptibility sensor (SUMS), which are respectively used to detect borehole magnetic polarity transitions and susceptibility variations. The NMRS measures the frequency of proton precession between a calibrated applied polarizing field and the earth's magnetic field that is proportional to the total field intensity of the earth. An average precision of 0.5 nT is based on duplicate runs. Its sensitivity is about 10^{-2} nT. The SUMS (Susceptibility Magnetic Sonde) measures mutual inductance caused by the surrounding borehole lithology using a transmitter coil and a receiver coil separated as a two-coil induction sonde. The operating frequency is about 200 Hz. The precision between duplicate runs is generally better than 3 ppm (3×10^{-6} SI), and the sensitivity of the sonde is almost 10^{-6} units. Data are recorded every 5 cm.

Magnetic induction **B** in a borehole depends on position p and time t (Pozzi et al., 1988) with:

$$\mathbf{B}(p,t) = \mathbf{Br}(p) + \mathbf{Ba}(p) + \mathbf{Bf}(p) + \mathbf{Bt}(p,t)$$

where $\mathbf{Br}(p)$ is the dipolar Earth's field and $\mathbf{Ba}(p)$ is the anomaly field related to large scale heterogeneities in susceptibility or in magnetic remanence. In the absence of such heterogeneities, the spatial variation of **Br** with depth is linear. $\mathbf{Bf}(p)$ is the induction due to the magnetization (induced and remanent) of the sediments around the borehole, and it can be easily separated from $\mathbf{Br}(p)$ and $\mathbf{Ba}(p)$ by subtracting the Earth's magnetic field gradient and by applying a high-pass filter. $\mathbf{Bt}(p,t)$ is time dependent and represents the induction caused by transient variations of the Earth's magnetic field. At sea, the time-dependent component can be estimated by repeat sections. To obtain direct magnetostratigraphy from $\mathbf{Bf}(p)$, the susceptibility and the total field measurements are combined to discriminate the induced and remanent magnetizations. Specifications of the probes, such as impulse response, calibration ratio, and geomagnetic location of the hole, are used to calculate the susceptibility effect on the scalar total field magnetometer. From these data the scalar remanent magnetization can be calculated.

The GHMT tool with its high vertical resolution was of considerable use in core-log integration by comparing it with the magnetic susceptibility measurements made on the multisensor track (MST).

Synthetic Seismograms

Synthetic seismograms were generated from acoustic impedance logs. Acoustic impedance is the product of *P*-wave velocity and the formation density, thus the interval transit-time log (from the SDT tool) and the density log (from the HLDT tool) are used. Reflection of a vertically incident seismic wave at an interface depends upon the difference in acoustic impedances across the interface divided by their sum. To produce the synthetic seismograms, impedance vs. depth logs are converted to impedance vs. two-way traveltime, and convolved with wavelets, which may be derived from actual seismic lines or from theoretical constructions like the standard zero-phase Ricker wavelet. The dominant frequency of the wavelet varies, depending on the source used in the original seismic profile. Vertical resolution is dependent on interval velocity and peak source frequency; thus the vertical resolution of a 30-Hz wavelet is about 15–30 m (for interval velocities from 1800 to 3600 m/s). Reflections cannot be generally resolved from smaller scale lithological units; however, through interference effects, thin beds can produce reflections that may be misinterpreted as major lithological changes.

Synthetic seismograms derived from borehole logging were compared to site-survey seismic profiles across the sites to correlate the regional seismic profiles to the borehole geology.

Log Processing

Processing, quality control, and display of the logging data were performed at each of the six holes logged during Leg 161 using Schlumberger "Logos" software and additional programs developed by members of the BRG. Displays of most of these processed data appear with accompanying text at the end of the appropriate site chapters in this volume. Files of all processed logs (including FMS, dipmeter, BRG temperature data, high-resolution density and neutron data, and sonic waveforms not shown in printed form) and explanatory text are included on the CD-ROM enclosed in the back pocket of this volume; a directory of the contents of the CD is found at the front of this volume.

Post-cruise shore-based processing of data from each hole consisted of: (1) depth adjustments of all logs to a common measurement below the seafloor; (2) corrections specific to certain tools; and (3) quality control and rejection of unrealistic values.

The depth shifting procedure is based on an interactive, graphical depth-match program that allows the processor to visually correlate logs and define appropriate shifts. The reference log and the log to be adjusted in depth are displayed side-by-side on a screen, and vectors connect the two at positions chosen by the user. The total gamma-ray curve (SGR) from the NGT run on each logging string was used in most cases to correlate the logging runs. In general, the reference curve is chosen on the basis of constant, low cable tension and high cable speed (tools run at faster speeds are less likely to stick and are less susceptible to data degradation caused by ship heave). Other factors, however, such as the length of the logged interval, presence of bottom hole assembly, and the statistical quality of the collected data (better statistics are obtained at lower logging speeds) are also considered in the selection. A list of the amount of differential depth shifts applied at each hole is available upon request to BRG (L-DEO).

Specific tool corrections were performed on the gamma-ray data to account for changes in borehole size and for the composition of the drilling fluid. Processing techniques unique to the AACT and GST tools of the geochemical string are described in detail below.

Quality control was performed by cross-correlation of all logging data. If the data processor concluded that individual log measurements represented unrealistic values, the choices were to either discard the data outright and substitute the null value of "–999.25," or identify a specific depth interval containing suspect values that must be used with caution. The latter are noted in the text that accompanies all processed log displays. Quality control of the acoustic data was based on discarding any of the four independent transit time measurements that were negative or that fell outside a range of reasonable values selected by the processor.

In addition to the standard 15.24 cm sampling rate, bulk density and neutron data were recorded at a sampling rate of 2.54 and 5.08 cm, respectively. While in normal processing short-spacing data are smoothed to match the long-spacing one, in enhanced processing this is reversed. In a situation where there is good contact between the HLDT pad and the borehole wall (low density correction) the results are improved, because the short-spacing data have better vertical resolution.

Locally, some intervals of log data appeared unreliable (usually due to poor hole conditions) and were not processed beyond what had been done onboard the ship. In general, a large (>12 in) and/or irregular borehole affects most recordings, particularly those that require eccentralization (HLDT) and a good contact with the borehole wall. Hole deviation can also degrade the data; the FMS, for example, is not designed to be run in holes that are more than 10° off the vertical, as the tool weight might cause the caliper to close.

Data Reduction

The well-log data from the Schlumberger tools are transmitted digitally up a wireline and are recorded and processed on the *JOIDES Resolution* in the Schlumberger Cyber Service Unit (CSU). The results from the CSU are made available as "field logs" for initial, shipboard interpretation. Subsequent reprocessing is necessary to correct the data for the effects of fluids added to the well, logging speed, and drill-pipe interference. Processing of the spectrometry data is required to transform the relative elemental yields into oxide weight fractions. The processing is performed with a set of log-interpretation programs written by Schlumberger but has been slightly modified to account for the lithologies and hole conditions encountered in ODP holes. The processing steps are summarized below:

Step 1: Reconstruction of Relative Elemental Yields From Recorded Spectral Data

This first processing step compares the measured spectra from the gamma-ray spectrometry tool with a series of "standard" spectra to determine the relative contribution (or yield) of each element. These "standards" approximate the spectrum of each element. Using a weighted, least-squares inversion method, the relative elemental yields are calculated at each depth level.

Six elemental standards (Si, Fe, Ca, S, Cl, and H) are used to produce the shipboard yields, but three additional standards (Ti, Gd, and K) can be included in the post-cruise processing to improve the fit of the spectral standards to the measured spectra (Grau and Schweitzer, 1989). The ability to detect an element is principally dependent on the size of its capture cross section and its abundance in the formation. Although Ti, Gd, and K often appear in the formation in very low concentrations, they can make a significant contribution to the measured spectra because they have large neutron-capture cross sections. Gd for example, has a capture cross section of 49,000 barns, whereas that of Si is 0.16 barns (Hertzog et al., 1987). Therefore, including Gd is necessary when calculating the best fit of the standard spectra to the measured spectrum, even though it typical concentration is only a few ppm.

The elemental standards (Si, Ca, Fe, Ti, Gd, K, Cl, and H) were used in the spectral analysis step for Holes 974C, 975C and 976B. The spectral standard for S was not used in the final analysis because

its inclusion in the spectral inversion was found to increase the noise level in the other elemental yields. A linear ten point (5 ft, 1.52 m) moving average was applied to the output elemental yields to increase the signal to noise ratios.

Step 2: Depth-Shifting

Geochemical processing involves the integration of data from the different tool strings; consequently, it is important that all the data are depth-correlated to one reference logging run. The NGT, run on each of the logging tool strings, provides a spectral gamma-ray curve with which to correlate each of the logging runs. A reference run is chosen on the basis of constant and low cable tension, and high cable speed (tools run at faster speeds are less likely to stick and are less susceptible to data degradation caused by ship heave). The depth-shifting procedure involves picking a number of reference points based on similar log character and then invoking a program which expands and compresses the matching logging run to fit the reference logging run. The main run of the quad combination tool string was chosen as the reference run for Holes 974C, 975C, and 976B on Leg 161.

Step 3: Calculation of Total Radioactivity and Th, U, and K Concentrations

The third processing routine calculates the total natural gamma-ray radiation in the formation, as well as concentrations of Th, U, and K, using the counts in five spectral windows from the NGT (Lock and Hoyer, 1971). This routine resembles shipboard processing; however, the results are improved during post-cruise processing by including corrections for hole-size changes and temperature variations. A Kalman filtering (Ruckebusch, 1983) is used in the CSU processing at sea to minimize the statistical uncertainties in the logs, which can otherwise create erroneous negative values and anti-correlation (especially between Th and U). An alpha filter has been introduced more recently and is now recommended by Schlumberger for shore-based processing. This filter strongly smooths the raw spectral counts but keeps the total gamma-ray curve unsmoothed before calculating out the Th, U, and K. The outputs of this program are K (wet wt%), U (ppm), and Th (ppm), as well as total gamma-ray and computed gamma-ray (total gamma ray minus U contribution). They are displayed as a function of depth in the log summary figures at the end of the relevant site chapter.

Step 4: Calculation of Al Concentration

The fourth processing routine (PREACT) calculates the concentration of Al in the formation using recorded gamma-ray data from four energy windows on the AACT. During this step, corrections are made for natural radioactivity, borehole-fluid neutron-capture cross section, formation neutron-capture cross section, formation slowing-down length, and borehole size. Porosity and density logs are needed as inputs in this routine to convert the wet-weight percentages of K and Al curves to dryweight percentages. To derive the best porosity log, shipboard core porosity measurements were compared with porosity logs calculated from the resistivity (using the relationship of Archie, 1942) and bulk density logs, and taken from the neutron porosity tool. The best correlation with core was found with the resistivity derived porosity for all 3 holes and this was used in the PREACT routine. A correction is also made for Si interference with Al; the ^{252}Cf source activates the Si, producing the aluminum isotope ^{28}Al (Hertzog et al., 1987). The program uses the Si yield from the GST to determine the Si background correction. The program outputs dry-weight percentages of Al and K which are combined in the next processing step with the GST-derived elemental yields in the oxide closure model.

Step 5: Normalization of Elemental Yields from the GST to Calculate the Elemental Weight Fractions

Relative concentrations of the GST-derived elemental yields can be determined by dividing each elemental yield by a relative spectral sensitivity factor (S_i). This factor is principally related to the thermal neutron-capture cross sections and also to its gamma-ray production and detection probability of each element (Hertzog et al., 1987). The relative elemental concentrations are related to the desired absolute concentrations by a depth-dependent normalization factor (F), as defined by the relationship:

$$Wt_i = FY_i / S_i \qquad (1)$$

where

Wt_i = absolute elemental concentration,
Y_i = relative elemental yield.

The normalization factor is calculated on the basis that the sum of all the elemental weight fractions is unity (100%). The closure model handles the absence of carbon and oxygen, which are not measured by this tool string, with the approximation that each of the measurable elements combines with a known oxide or carbonate. The dry weight percent of Al and K are normalized with the reconstructed elemental yields to the determine the normalization factor at each depth interval from the following equation:

$$F(\Sigma_i X_i Y_i / S_i) + X_k Wt_k + X_{Al} Wt_{Al} = 100, \qquad (2)$$

where

X_i = oxide factor; atomic weight of the associated oxide or carbonate of element i ÷ atomic weight of element i,
X_k = oxide factor; atomic weight K_2O ÷ atomic weight of K,
Wt_k = dry-weight % of K as determined from the NGT,
X_{Al} = oxide factor; atomic weight of Al_2O_3 ÷ atomic weight of Al, and
Wt_{Al} = dry-weight % of Al, as determined from the AACT.

The value, X_i, accounts for the C and O associated with each element. Table 9 lists the oxide factors used in this calculation for Holes 974C, 975C, and 976B.

Step 6: Calculation of Oxide Percentages

This routine converts the elemental weight percentages into oxide percentages by multiplying each by its associated oxide factor, as shown in Table 9. The results are displayed as a function of depth in the log summary figures at the end of the relevant site chapter. The results are compared to the calcium carbonate measurements per-

Table 9. Oxide factors used in normalizing elements to 100% and converting elements to oxides.

Element	Oxide/carbonate	Conversion factor (Holes 974C, 975C)	Conversion factor (Hole 976B)
Si	SiO$_2$	2.139	2.139
Ca	CaCO$_3$	2.497	1.399
Fe	FeO*	1.358	1.358
K	K$_2$O	1.205	1.205
Ti	TiO$_2$	1.668	1.688
Al	Al$_2$O$_3$	1.889	1.889

formed on board for Holes 974C and 975C and to the XRF measurements for Hole 976B.

Step 7: Calculation of Error Logs

The statistical uncertainty of each element is calculated for each of the elements measured with the GST and NGT (Grau et al., 1990; Schweitzer et al., 1988; Bristow et al., 1994). This error is strongly related to the normalization factor, which is calculated at each depth level (Equation 2). The normalization factor is displayed to the right of the logs in the log summary figures at the end of the relevant site chapter. A lower normalization factor represents better counting statistics and therefore higher quality data.

IN SITU TEMPERATURE MEASUREMENTS

Downhole temperature measurements were taken on Leg 161 for two purposes: (1) to study the thermal evolution of the organic-rich sediments in the deeper basins of the Western Mediterranean, an (2) to determine regional variations in heat flow in the Alboran Basin.

In situ temperature measurements were made with two different tools: the ADARA tool, used with the APC coring shoe as a part of the regular coring operations; and the Water Sampler Temperature Probe (WSTP) tool deployed separately during Extended Core Barrel (XCB) drilling.

These data were combined with measurements of thermal conductivity on recovered core samples (see "Physical Properties" section, this chapter) to yield the heat flow values. Downhole temperature logs were also obtained during the downhole logging (see "Downhole Logging" section, this chapter).

APC Tool (ADARA) Temperature Measurements

The ADARA tool was used to obtain in situ sediment temperatures during piston-coring operations. The components of the thermal tool are contained in an annulus in the coring shoe, and include a platinum temperature sensor and a data logger. The platinum resistance temperature device (RTD) is calibrated over a range of −20° to 100°C, with resolution of 0.01°C. In operation, the coring shoe was mounted on a core barrel and lowered down the pipe by wireline. The tool was typically held for 5−10 minutes at the mudline to equilibrate with bottom-water temperatures and then lowered to the end of the drill string. Standard APC coring techniques were used, with the core barrel being fired out through the drill bit using hydraulic pressure. The ADARA tool is then left in the sediment for 10−15 minutes to obtain a temperature record. This provided a sufficiently long transient record for reliable extrapolation of the steady-state temperature. The nominal accuracy of the unreduced temperature measurements is estimated to be 0.1°C.

Water-Sampling Temperature Probe (WSTP) Temperature Measurements

The WSTP provides downhole temperature measurements in sediments not yet affected by mechanical drilling disturbance or borehole fluid circulation. The WSTPs aboard the *JOIDES Resolution* are based on the Uyeda temperature tool (Yokota et al., 1980). One WSTP instrument includes a Barnes fluid sampler (Barnes, 1979) in order to combine pore-fluid sampling and downhole temperature measurements on a single downhole wireline run. The WSTP tools on the *JOIDES Resolution* have been periodically upgraded and redesigned since ODP Leg 110. Most important, they were modified to have a stouter thermal probe (Barnes, 1988), increased resistance to corrosive downhole fluids, and improved isolation of the tool elec-
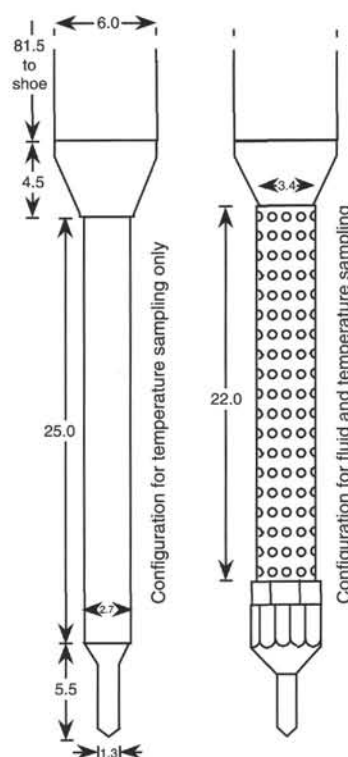

Figure 18. Schematic diagram of the WSTP thermal probe and water sampler. All dimensions are in centimeters. Taken from Davis et al., 1992.

tronics from the probe tip. These modifications required removal of the downhole pressure sensor that was available on earlier versions of the tool.

The WSTP is mounted in a standard coring barrel, with a narrow stainless steel probe extending 1.1 m beyond the end of the barrel (Fig. 18). The probe contains the thermistor used during temperature measurements, as well as the filtering system for obtaining the pore-fluid sample when configured for water sampling. In operation, the WSTP is lowered down the drill pipe by wireline while the drill bit is held slightly off the bottom of the hole. The descent of the WSTP is halted for 10 to 15 minutes at the mudline to allow the probe to equilibrate with bottom temperatures. The tool is then lowered to the bottom of the drill string, where it is latched into place with the probe extending through the center of the drill bit. The drill string is lowered even more, forcing the probe into the sediments at the bottom of the hole. Temperature measurements are recorded every 4.369 seconds. With an APC/XCB bottom-hole assembly, the bit can be decoupled from the tool after penetration so that the probe will not be disturbed by drillstring heave. The driller can continuously circulate fluid during the station if necessary to keep the hole clear of fill, as circulation of cold bottom water in the hole will have little influence on measured temperatures at times less than a few hours after drilling, so long as the probe penetrates at least 50 cm (Fisher and Hounslow, 1990). If taken, fluid samples were not drawn until the probe had been in place for 15 min, because the influx of fluids may bias the temperature measurements.

In practice, equilibrium formation temperatures are never measured because the thermal state of the tool and the formation are disturbed by insertion of the probe. The period required for the sediments and probe to equilibrate is prohibitively long, so the steady-state temperature must be estimated by extrapolating the transient thermal signal recorded by the probe (Fig. 19). On Leg 161,
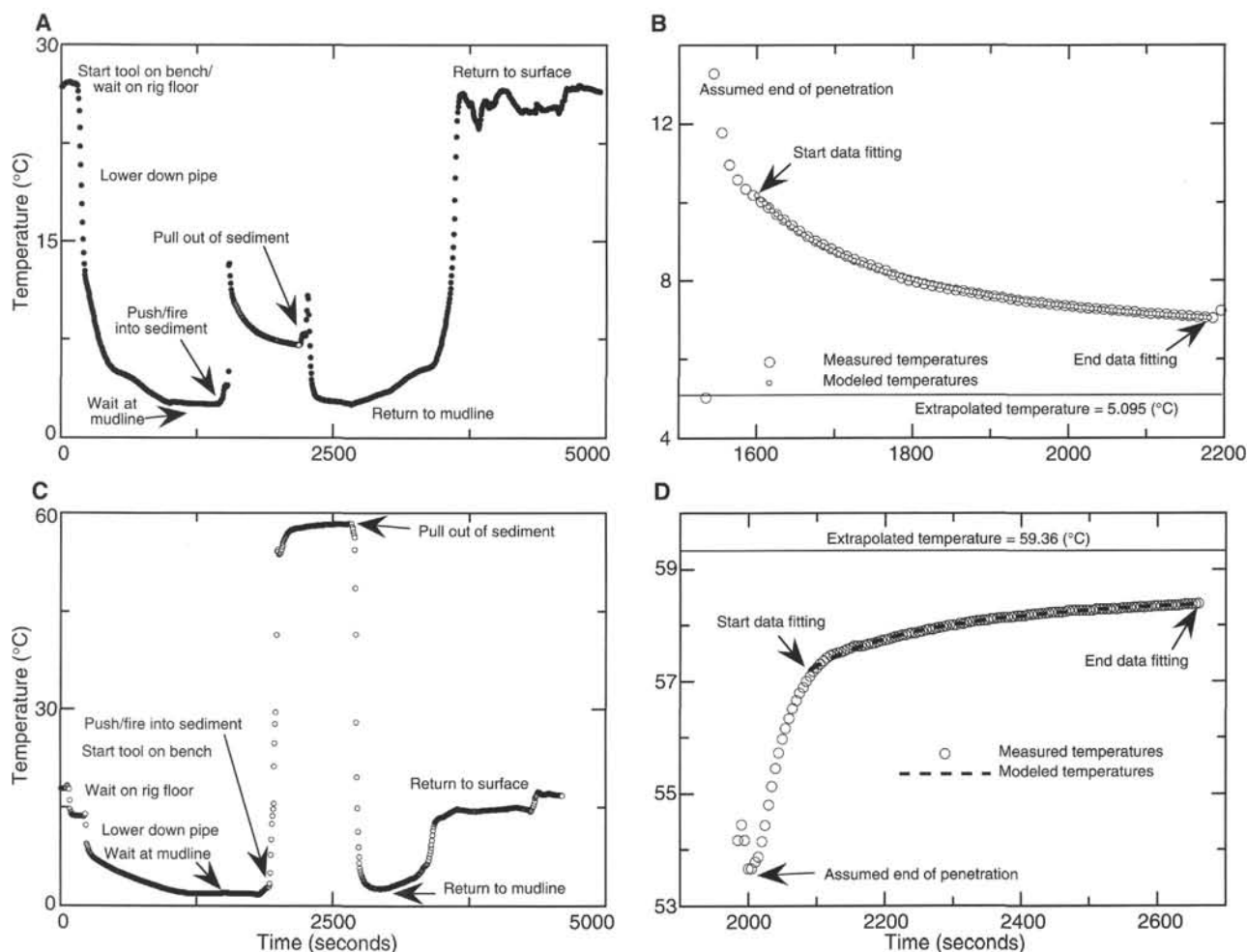
Figure 19. Examples of temperature/time and curve-fit records. **A.** A good temperature/time record for a measurement in relatively cool sediments. The heat pulse resulting from insertion of the probe is clearly visible. The WSTP probe is pushed into the sediments, while the APC tool is fired into the sediments as part of the core barrel. **B.** Measured and modeled temperatures from the same run as in A. The modeled temperature curve extrapolates to 5.095°C. **C.** A good temperature/time record for a measurement in warm sediments. The frictional heat pulse is barely apparent. **D.** Measured and modeled temperatures from the same run as in C. The modeled curve extrapolates to an undisturbed temperature of 59.36°C.

equilibrium temperatures were estimated from 10–15-min records of the transient temperature using the standard processing software.

Several potential sources of error contribute to limiting the accuracy of the equilibrium temperature estimated from the WSTP data. First, the probe heating at insertion is not instantaneous as the processing software assumes. Since the time of insertion is not known with great precision, this causes some uncertainty in the duration of the transient thermal signal. In practice, this problem was resolved by applying an empirical time shift to the thermal data in such a way as to best fit the theoretical transient response functions of Bullard (1954). Secondly, the relatively short length of the narrow probe appears to allow only a few minutes of undisturbed measurements before a thermal disturbance is conducted down from the larger-diameter section above, limiting the accuracy of temperature extrapolations to about ±0.1–0.2°C. Also, because of its relative size and geometry, probe calibration is difficult and, consequently, only the thermistors can be calibrated, not the entire instrument. Finally, the probe may not always be completely inserted, may have been insert-ed into cuttings in the bottom of the borehole, or may have fractured the bottom-hole sediments upon insertion. However, it was possible to recognize the presence of such problems by the shape of the temperature-time curve. These data were not used. The combined effect of these uncertainties leads to an estimated accuracy of +0.05 to 0.1°C in the unreduced temperature measurements and +0.5 to 1°C error in the estimated equilibrium temperature. A review of thermal data obtained with this type of probe during the DSDP is given by Hyndman et al. (1987).

Data Reduction

The data reduction method for both the ADARA and WSTP temperature probes estimates the steady-state bottom-hole temperature by forward modeling the recorded transient temperature curve as a function of time. The shape of the transient temperature curve is determined by the response function of the tool and the thermal properties of the sediments (Bullard, 1954; Horai and Von Herzen, 1985).

In general, temperature increases following emplacement of the probe due to frictional heating of the probe tip during insertion. The temperature peaks after a short period of time and decreases monotonically thereafter, approaching the steady-state temperature of the sediments at a rate inversely proportional to time. Data-reduction software was used on Leg 161 to interactively fit modeled transient temperature curves for the tools to the observed data and extrapolate for the equilibrium temperature. Variables in the modeling method are the thermal conductivity of the sediments, tool insertion time, delay time between tool insertion and peak temperature, and the length of the portion of the curve to be fit.

The theoretical decay curves simulate the instantaneous heating (or cooling) of the sediment following probe penetration, but in practice a finite time is required for the sensors to reach a maximum temperature. As a result, the effective origin time of the thermal pulse is delayed as a function of tool and sediment properties. The temperature data are recorded with a finite sampling interval of a few seconds, so the precise time of penetration is unknown. An effective penetration time and an extrapolated temperature are estimated by shifting the time axis of the theoretical thermal decay curves to fit the actual data. Temperatures from the first 5–10 measurements following penetration commonly do not follow the theoretical curves, but later parts of the records usually provide a good fit (Fig. 19). The choice of which data should be included in the curve fitting, and which time shift should be used, is partly subjective; it is probably best to use as much of the actual decay curve as possible. The variations in extrapolated temperatures that result from choosing different time intervals and time shifts can be used to estimate errors associated with the temperatures finally assigned to represent in situ conditions. In practice, relatively few iterations of the modeling procedure were required to obtain reasonable fits to the temperature data that were consistent with the thermal conductivity measurements obtained as part of the routine physical properties analysis.

REFERENCES

American Society of Testing and Materials, 1989. *Annual Book of ASTM Standards for Soil and Rock; Building Stones:* Geotextiles (Vol. 04.08): Philadelphia (ASTM), 168–862.

Archie, G.E., 1942. The electrical resistivity log as an aid in determining some reservoir characteristics. *Trans. Am. Inst. Min. Metall. Pet. Eng.*, 146:54–62.

Barnes, R.O., 1979. Operation of the IPOD in-situ pore water sampler [Introduction and explanatory notes]. *In* Sibuet, J.-C., Ryan, W.B.F., et al., *Init. Repts. DSDP*, 47 (Pt. 2): Washington (U.S. Govt. Printing Office), 19–22.

————, 1988. ODP in-situ fluid sampling and measurement: a new wireline tool. *In* Mascle, A., Moore, J.C., et al., *Proc. ODP, Init. Repts.*, 110: College Station, TX (Ocean Drilling Program), 55–63.

Blatt, H., Middleton, G., and Murray, R., 1980. *Origin of Sedimentary Rocks* (2nd ed.): Englewood Cliffs, NJ (Prentice-Hall).

Bloemendal, J., Barton, C.E., and Radhakrishnamurthy, C., 1985. Correlation between Rayleigh loops and frequency-dependent and quadrature susceptibility: application to magnetic granulometry of rocks. *J. Geophys. Res.*, 90:8789–8792.

Bloemendal, J., King, J.W., Hall, F.R., and Doh, S.-J., 1992. Rock magnetism of late Neogene and Pleistocene deep-sea sediments: relationship to sediment source, diagenetic processes, and sediment lithology. *J. Geophys. Res.*, 97:4361–4375.

Blow, W.H., 1979. *The Cainozoic Globigerinida:* Leiden (E.J. Brill).

Borradaile, G.J., 1988. Magnetic susceptibility, petrofabrics and strain. *Tectonophysics*, 156:1–20.

Boyce, R.E., 1976. Definitions and laboratory techniques of compressional sound velocity parameters and wet-water content, wet-bulk density, and porosity parameters by gravimetric and gamma-ray attenuation techniques. *In* Schlanger, S.O., Jackson, E.D., et al., *Init. Repts. DSDP*, 33: Washington (U.S. Govt. Printing Office), 931–958.

Brassell, S.C., Eglinton, G., Marlowe, I.T., Pflaumann, U., and Sarnthein, M., 1986. Molecular stratigraphy: a new tool for climatic assessment. *Nature*, 320:129–133.

Bristow, J. F., Lofts, J. C., Harvey, P. K. and Lovell, M. A., 1994. Reservoir characterisation using nuclear geochemical logging. *Trans. 16th European Formation Evaluation Symposium*, Aberdeen.

Bullard, E.C., 1954. The flow of heat through the floor of the Atlantic Ocean. *Proc. R. Soc. London A*, 222:408–429.

Cande, S.C., and Kent, D.V., 1995. Revised calibration of the geomagnetic polarity timescale for the Late Cretaceous and Cenozoic. *J. Geophys. Res.*, 100:6093–6095.

Cita, M.B., 1975. Studi sul Pliocene e gli strati di passaggoi dal Miocene al Pliocene, VII. Planktonic foraminiferal biozonation of the Mediterranean Pliocene deep sea record: a revision. *Riv. Ital. Paleontol. Stratigr.*, 81:527–544.

Courtney, R.C., and Mayer, L.A., 1993. Calculating acoustic parameter by a filter correlation method. *J. Acoust. Soc. Am.*, 93:1145–1154.

Cox, K.G., Bell, J.D., and Pankhurst, R.J., 1979. *The Interpretation of Igneous Rocks:* London (Allen and Unwin).

Davis, E.E., Mottl, M.J., Fisher, A.T., et al., 1992. *Proc. ODP, Init. Repts.*, 139: College Station, TX (Ocean Drilling Program).

de Kaenel, E., and Villa, G., in press. Oligocene–Miocene calcareous biostratigraphy and paleoecology from the Iberia Abyssal Plain. *In* Whitmarsh, R.B., Sawyer, D.S., Klaus, A., and Masson, D.G. (Eds.), *Proc. ODP, Sci. Results*, 149: College Station, TX (Ocean Drilling Program).

Dunham, R.J., 1962. Classification of carbonate rocks according to depositional texture. *In* Ham, W.E. (Ed.), *Classification of Carbonate Rocks.* AAPG Mem., 108–121.

Ellis, D.V., 1987. *Well Logging For Earth Scientists:* Amsterdam (Elsevier).

Ellwood, B.B., Hrouda, F., and Wagner, J.-J., 1988. Symposia on magnetic fabrics: introductory comments. *Phys. Earth Planet. Inter.*, 51:249–252.

Embry, A.F., and Klovan, J.E., 1971. A late Devonian reef tract on northeastern Banks Island, Northwest Territories. *Bull. Can. Pet. Geol.*, 19:730–781.

Espitalié, J., Deroo, G., and Marquis, F., 1986. La pyrolyse Rock-Eval et ses applications, Partie III. *Rev. Inst. Fr. Pet.*, 41:73–89.

Fisher, A.T., and Hounslow, M.W., 1990. Heat flow through the toe of the Barbados accretionary complex. *In* Moore, J.C., Mascle, A., et al., *Proc. ODP, Sci. Results*, 110: College Station, TX (Ocean Drilling Program), 345–363.

Fisher, R.V., and Schmincke, H.-U., 1984. *Pyroclastic Rocks:* New York (Springer-Verlag).

Foresi, L., Iaccarino, S., Mazzei, R., and Salvatorini, G., in press. New data on the calcareous plankton biostratigraphy of the middle to upper Miocene at the Mediterranean area. *Riv. Ital. Paleont. Stratigr.*

Gieskes, J.M., Gamo, T., and Brumsack, H., 1991. Chemical methods for interstitial water analysis aboard *JOIDES Resolution. ODP Tech. Note*, 15.

Grau, J.A., and Schweitzer, J.S., 1989. Elemental concentrations from thermal neutron capture gamma-ray spectra in geological formations. *Nucl. Geophys.*, 3:1–9.

Grau, J.A., Schweitzer, J.S., and Hertzog, R.C., 1990. Statistical uncertainties of elemental concentrations extracted from neutron-induced gamma-ray measurements. *IEEE Trans. Nucl. Sci.*, 37:2175–2178.

Hagelberg, T., Shackleton, N., Pisias, N., and Shipboard Scientific Party, 1992. Development of composite depth sections for Sites 844 through 854. *In* Mayer, L., Pisias, N., Janecek, T., et al., *Proc. ODP, Init. Repts.*, 138 (Pt. 1): College Station, TX (Ocean Drilling Program), 79–85.

Hamilton, E.L., 1971. Elastic properties of marine sediments. *J. Geophys. Res.*, 76:579–604.

Hasegawa, S., Sprovieri, R., and Poluzzi, A, 1990. Quantitative analyses of benthic foraminiferal assemblages from Plio-Pleistocene sequence in the Tyrrhenian Sea, ODP Leg 107. *In* Kastens, K., Mascle J., et al., 1990. *Proc. ODP, Sci. Results*, 107: College Station, TX (Ocean Drilling Program), 461–478.

Hemleben, C., Spindler, M., and Anderson, O.R., 1989. *Modern Planktonic Foraminifera:* Berlin (Springer-Verlag).

Hertzog, R.C., Colson, J.L., Seeman, B., O'Brien, M.S., Scott, H.D., McKeon, D.C., Wraight, P.D., Grau, J.A., Ellis, D.V., Schweitzer, J.S., and Herron, M.M., 1987. Geochemical logging with spectrometry tools. *SPE Form. Eval.*, 62:447–460.

Hilgen, F.J., 1991. Extension of the astronomically calibrated (polarity) time scale to the Miocene/Pliocene boundary. *Earth Planet. Sci. Lett.*, 107:349–368.

Horai, K., and Von Herzen, R.P., 1985. Measurement of heat flow on Leg 86 of the Deep Sea Drilling Project. *In* Heath, G.R., Burckle, L.H., et al., *Init. Repts. DSDP*, 86: Washington (U.S. Govt. Printing Office), 759–777.

Hrouda, F., 1982. Magnetic anisotropy of rocks and its application in geology and geophysics. *Geophys. Surv.*, 5:37–82.

Hyndman, R.D., Langseth, M.G., and Von Herzen, R.P., 1987. Deep Sea Drilling Project geothermal measurements: a review. *Rev. Geophys.*, 25:1563–1582.

Iaccarino, S., 1985. Mediterranean Miocene and Pliocene planktic foraminifera. *In* Bolli, H.M., Saunders, J.B., and Perch-Nielsen, K. (Eds), *Plankton Stratigraphy:* Cambridge (Cambridge Univ. Press), 283–314.

Johnson, H.P., Lowrie, W., and Kent, D.V., 1975. Stability of anhysteretic remanent magnetization in fine and coarse magnetite and maghemite particles. *Geophys. J. R. Astron. Soc.*, 41:1–10.

Karlak, R.F., and Burnett, D.S., 1966. Quantitative phase analysis by X-ray diffraction. *Anal. Chem.*, 38:421–443.

Kidd, R.B., Cita, M.B., and Ryan, W.B.F., 1978. Stratigraphy of eastern Mediterranean sapropel sequences recovered during DSDP Leg 42A and their paleoenvironmental significance. *In* Hsü, K.J., Montadert, L., et al., *Init. Repts. DSDP*, 42 (Pt. 1): Washington (U.S. Govt. Printing Office), 421–443.

Krijgsman, W., Hilgen, F.J., Langereis, C.G., Santarelli, A., and Zachariasse, W.J., in press. Late Miocene magnetostratigraphy, biostratigraphy and cyclostratigraphy in the Mediterranean. *Earth Planet. Sci. Lett.*

Kvenvolden, K.A., and McDonald, T.J., 1986. Organic geochemistry on the *JOIDES Resolution*—an assay. *ODP Tech. Note*, 6.

Le Maitre, R.W., 1976. The chemical variability of some common igneous rocks. *J. Petrol.*, 17:589–637.

Le Maitre, R.W., 1989. *A Classification of Igneous Rocks and Glossary of Terms:* Oxford (IUGS, Blackwell).

Lock, G.A., and Hoyer, W.A., 1971. Natural gamma-ray spectral logging. *Log Analyst*, 12:3–9.

Lowrie, W., 1990. Identification of ferromagnetic minerals in a rock by coercivity and unblocking temperature properties. *Geophys. Res. Lett.*, 17:159–162.

MacKenzie, W.S., Donaldson, C.H., and Guilford, C., 1982. *Atlas of Igneous Rocks and Their Textures:* New York (Wiley).

MacLeod, C.J., Parson, L.M., and Sager, W.W., 1994. Reorientation of cores using the Formation MicroScanner and Borehole Televiewer: application to structural and paleomagnetic studies with the Ocean Drilling Program. *In* Hawkins, J., Parson, L., Allan, J., et al., *Proc. ODP, Sci. Results*, 135: College Station, TX (Ocean Drilling Program), 301–311.

MacLeod, C.J., Parson, L.M., Sager, W.W., and the ODP Leg 135 Scientific Party, 1992. Identification of tectonic rotations in boreholes by the integration of core information with Formation MicroScanner and Borehole Televiewer images. *In* Hurst, A., Griffiths, C.M., and Worthington, P.F. (Eds.), *Geological Applications of Wireline Logs II.* Geol. Soc. Spec. Publ. London, 65:235–246.

Maher, B.A., 1988. Magnetic properties of some synthetic sub-micron magnetites. *Geophys. J. R. Astron. Soc.*, 94:83–96.

Manheim, F.T., and Sayles, F.L., 1974. Composition and origin of interstitial waters of marine sediments based on deep sea drill cores. *In* Goldberg, E.D. (Ed.), *The Sea* (Vol. 5): New York (Wiley Interscience), 527–568.

Martini, E., 1971. Standard Tertiary and Quaternary calcareous nannoplankton zonation. *In* Farinacci, A. (Ed.), *Proc. 2nd Int. Conf. Planktonic Microfossils Roma:* Rome (Ed. Tecnosci.), 2:739–785.

Mayer, L.A., Courtney, R.C., and Moran, K., 1988. Ultrasonic measurements of marine sediment properties. *Prog. Oceanogr.*, 87:1–139.

Mazzullo, J.M., Meyer, A., and Kidd, R.B., 1988. New sediment classification scheme for the Ocean Drilling Program. *In* Mazzullo, J., and Graham, A.G., *Handbook for Shipboard Sedimentologists.* ODP Tech. Note, 8:45–67.

Munsell Soil Color Charts, 1975. Baltimore (Munsell Color).

Peccerillo, A., and Taylor, S.R., 1976. Geochemistry of Eocene calc-alkaline volcanic rocks from the Kastamonu area, northern Turkey. *Contrib. Mineral. Petrol.*, 58:63–81.

Peters, K.E., 1986. Guidelines for evaluating petroleum source rock using programmed pyrolysis. *AAPG Bull.*, 70:318–329.

Pozzi, J.-P., Martin, J.P., Pocachard, J., Feinberg, H., and Galdeano, A., 1988. In situ magnetostratigraphy: interpretation of magnetic logging in sediments. *Earth Planet. Sci. Lett.*, 88:357–373.

Prahl, F.G., and Wakeham, S.G., 1987. Calibration of unsaturation patterns in long-chain ketone compositions for paleotemperature assessment. *Nature*, 330:367–369.

Pratson, E.L., Broglia, C., and Jarrard, R., 1993. Data report: Geochemical well logs through Cenozoic and Quaternary sediments from Sites 815, 817, 820, 822, and 823. *In* McKenzie, J.A., Davies, P.J., Palmer-Julson, A., et al., *Proc. ODP, Sci. Results*, 133: College Station, TX (Ocean Drilling Program).

Prell, W.L., Niitsuma, N., et al., 1989. *Proc. ODP, Init. Repts.*, 117: College Station, TX (Ocean Drilling Program).

Rio, D., Raffi, I., and Villa, G., 1990. Pliocene-Pleistocene calcareous nannofossil distribution patterns in the Western Mediterranean. *In* Kastens, K.A., Mascle, J., et al., *Proc. ODP, Sci. Results*, 107: College Station, TX (Ocean Drilling Program), 513–533.

Rio, D., Sprovieri, R., and Di Stefano, E., 1994. The Gelasian stage: a proposal for a new chronostratigraphic unit of the Pliocene series. *Riv. Ital. Paleontol. Stratigr.*, 100:103–124.

Roth, P.H., and Thierstein, H., 1972. Calcareous nannoplankton: Leg 14 of the Deep Sea Drilling Project. *In* Hayes, D.E., Pimm, A.C., et al., *Init. Repts. DSDP*, 14: Washington (U.S. Govt. Printing Office), 421–485.

Ruckebusch, G., 1983. A Kalman filtering approach to natural gamma ray spectroscopy in well logging. *IEEE Trans. Autom. Control*, AC-28:372–380.

Sass, J.H., Kennelly, J.P., Jr., Smith, E.P., and Wendt, W.E., 1984. Laboratory line-source methods for the measurement of thermal conductivity of rocks near room temperature. *Open-File Rep.—U.S. Geol. Surv.*, 84-0091.

Schlumberger, 1989. *Log Interpretation Principles/Applications:* Houston, TX (Schlumberger Educ. Services).

Schmid, R., 1981. Descriptive nomenclature and classification of pyroclastic deposits and fragments: recommendation of the IUGS Subcommission on the Systematics of Igneous Rocks. *Geology*, 9:41–43.

Schweitzer, J.S., Grau, J.A., and Hertzog, R.C., 1988. Precision and accuracy of short-lived activation measurements for in situ geological analyses. *J. Trace Microprobe Techniques*, 6:437–451.

Scott, H.D., and Smith, M.P., 1973. The aluminum activation log. *Log Analyst*, 14:3–12.

Shackleton, N.J., Baldauf, J.G., Flores, J.-A., Iwai, M., Moore, T.C. Jr., Raffi, I., and Vincent, E., 1995. Biostratigraphic summary for Leg 138. *In* Pisias, N.G., Mayer, L.A., Janecek, T.R., Palmer-Julson, A., and van Andel, T.H. (Eds.) *Proc. ODP, Sci. Results*, 138: College Station, TX (Ocean Drilling Program), 517–536.

Shelley, D., 1983. *Igneous and Metamorphic Rocks Under the Microscope: Classification, Textures, Microstructures and Mineral Preferred Orientations:* London (Chapman and Hall).

Shepard, F., 1954. Nomenclature based on sand-silt-clay ratios. *J. Sediment. Petrol.*, 24:151–158.

Shipboard Scientific Party, 1990. Explanatory notes. *In* Rangin, C., Silver, E., von Breymann, M.T., et al., *Proc. ODP, Init. Repts.*, 124: College Station, TX (Ocean Drilling Program), 7–33.

————, 1991. Explanatory notes. *In* Davies, P.J., McKenzie, J.A., Palmer-Julson, A., et al., *Proc. ODP, Init. Repts.*, 133 (Pt. 1): College Station, TX (Ocean Drilling Program), 31–58.

————, 1992. Explanatory notes. *In* Collot, J.-Y., Greene, H.G., Stokking, L.B., et al., *Proc. ODP, Init. Repts.*, 134: College Station, TX (Ocean Drilling Program), 65–91.

————, 1993. Explanatory notes. *In* Rea, D.K., Basov, I.A., Janecek, T.R., Palmer-Julson, A., et al., *Proc. ODP, Init. Repts.*, 145: College Station, TX (Ocean Drilling Program), 9–33.

————, 1995a. Explanatory notes. *In* Curry, W.B., Shackleton, N.J., Richter, C., et al., *Proc. ODP, Init. Repts.*, 154: College Station, TX (Ocean Drilling Program), 11–38.

————, 1995b. Explanatory notes. *In* Flood, R.D., Piper, D.J.W., Klaus, A., et al., *Proc. ODP, Init. Repts.*, 155: College Station, TX (Ocean Drilling Program), 47–81.

—————, 1995c. Site 926. *In* Curry, W.B., Shackleton, N.J., Richter, C., et al., *Proc. ODP, Init. Repts.,* 154: College Station, TX (Ocean Drilling Program), 153–232.

—————, 1996. Site 960. *In* Mascle, J., Lohmann, G.P., Clift, P.D., et al., *Proc. ODP, Init. Repts.,* 159: College Station, TX (Ocean Drilling Program), 151–215.

—————, in press. Explanatory notes. *In* Emeis, K.-C., Robertson, A.H.F., Richter, C., et al., *Proc. ODP Init. Repts.,* 160: College Station, TX (Ocean Drilling Program).

Sprovieri, R., 1992. Mediterranean Pliocene biochronology: a high resolution record based on quantitative planktonic foraminifera distribution. *Riv. Ital. Paleontol. Stratigr.,* 98:61–100.

—————, 1993. Pliocene–early Pleistocene astronomically forced planktonic foraminifera abundance fluctuations and chronology of Mediterranean calcareous plankton bio-events. *Riv. Ital. Paleontol. Stratigr.,* 99:371–414.

Theodoridis, S., 1984. Calcareous nannofossil biozonation of the Miocene and revision of the helicoliths and discoasters. *Utrecht Micropaleontol. Bull.,* 32:1–271.

Timur, A., and Toksöz, M.N., 1985. Downhole geophysical logging. *Annu. Rev. Earth Planet. Sci.,* 13:315–344.

Vacquier, V., 1985. The measurement of thermal conductivity of solids with a transient linear heat source on the plane surface of a poorly conducting body. *Earth Planet. Sci. Lett.,* 74:275–279.

Varol, O., 1989. Calcareous nannofossil study of the central and western Solomon Islands. *In* Vedder, J.G., and Bruns, T.R. (Eds.), *Geology and Offshore Resources of Pacific Island Arcs: Solomon Islands and Bouga-inville, Papua New Guinea Regions.* Circum-Pacific Council for Energy and Mineral Resources, Earth Sci. Ser., 12:239–268.

Von Herzen, R.P., and Maxwell, A.E., 1959. The measurements of thermal conductivity of deep-sea sediments by a needle probe method. *J. Geophys. Res.,* 64:1557–1563.

Wentworth, C.K., 1922. A scale of grade and class terms for clastic sediments. *J. Geol.,* 30:377–392.

Wilkens, R.H., DeCarlo, E.H., and Tribble, J.S., 1992. Data report: X-ray bulk mineralogy of Exmouth and Wombat Plateau sediments, northwest Australian Margin. *In* von Rad, U., Haq, B.U., et al., *Proc. ODP, Sci. Results,* 122: College Station, TX (Ocean Drilling Program), 887–896.

Wright, R., 1978. Neogene paleobathymetry of the Mediterranean based on benthic foraminifers from DSDP Leg 42. *In* Hsü, K.J., Montadert, L., et al., *Init. Repts. DSDP,* 42 (Pt. 1): Washington (U.S. Govt. Printing Office), 837–846.

Wyllie, M.R.J., Gregory, A.R., and Gardner, L.W., 1956. Elastic wave velocities in heterogeneous and porous media. *Geophysics,* 21:41–70.

Yokota, T., Kinoshita, H., and Uyeda, S., 1980. New DSDP (Deep Sea Drilling Project) downhole temperature probe utilizing IC RAM (memory) elements. *Bull. Earthquake Res. Inst., Univ. Tokyo,* 55:75–88.

Young, J.R., 1991. A Quaternary nannofossil range chart. *INA Newsl.,* 13:14–17.

Ms 161IR-102